Probing Ultralight Bosons with Binary Black Holes

Daniel Baumann,[1] Horng Sheng Chia,[1] and Rafael A. Porto[2,3,4]

[1] *Institute of Theoretical Physics, University of Amsterdam, Science Park 904, Amsterdam, 1098 XH, The Netherlands*

[2] *ICTP South American Institute for Fundamental Research, Rua Dr. Bento Teobaldo Ferraz 271, 01140-070 Sao Paulo, SP Brazil*

[3] *Deutsches Elektronen-Synchrotron DESY, Theory Group, D-22603 Hamburg, Germany*

[4] *Max Planck Institut für Gravitationsphysik (Albert Einstein Institute), Callinstr. 38, D-30167 Hannover, Germany*

Abstract

We study the gravitational-wave (GW) signatures of clouds of ultralight bosons around black holes (BHs) in binary inspirals. These clouds, which are formed via superradiance instabilities for rapidly rotating BHs, produce distinct effects in the population of BH masses and spins, and, for real fields, a continuous monochromatic GW signal. We show that the presence of a binary companion greatly enriches the dynamical evolution of the system, most remarkably through the existence of resonant transitions between the growing and decaying modes of the cloud (analogous to Rabi oscillations in atomic physics). These resonances have rich phenomenological implications for current and future GW detectors. Notably, the amplitude of the GW signal from the clouds may be reduced, and in many cases terminated, much before the binary merger. The presence of a boson cloud can also be revealed in the GW signal from the binary through the imprint of finite-size effects, such as spin-induced multipole moments and tidal Love numbers. The time dependence of the cloud's energy density during the resonance leads to a sharp feature, or at least attenuation, in the contribution from the finite-size terms to the waveforms. The observation of these effects would constrain the properties of putative ultralight bosons through precision GW data, offering new probes of physics beyond the Standard Model.

Contents

1 Introduction

The recent detections of gravitational waves (GWs) by the LIGO/Virgo collaboration [1–5] mark the beginning of multi-messenger astronomy [6] and the birth of 'precision gravity' [7, 8]. Binary systems, of comparable masses or extreme-mass ratios, will become the leading probe to test gravitational dynamics and the physics of compact objects, such as black holes (BHs) and neutron stars (NSs), under unique conditions. While it is indisputable that future GW observations will play a transformative role in astrophysics [9], it is less clear what impact these measurements will have on other branches of physics, and in particular, whether they can shed light on phenomena beyond the Standard Model. In principle, the non-perturbative regime of gravitational dynamics may carry imprints of 'new physics', see e.g. [10]. However, the need for numerical modelling, together with the small number of cycles involved, may hinder our ability to pinpoint different scenarios, if restricted only to the merger phase. In contrast, an accurate analytic reconstruction of the signal during the inspiral, in combination with simulations for the late stages of the coalescence, offers a unique opportunity to study physics beyond the Standard Model through GW precision data.

Using GW observations as probes of new physics is challenging, mainly due to the efficient decoupling of short-distance physics from long-distance observations. Indeed, finite-size effects, characterized by higher-derivative terms in a 'worldline' effective field theory (EFT) approach [11–22], encapsulate the physics at scales shorter than the size of the objects sourcing GWs in a binary system. Because Einstein gravity is derivatively coupled, these terms scale with high powers of the ratio between the size and the separation of the bodies. For a non-rotating compact object, the first correction to the structureless point-particle approximation is due to tidal effects and scales with the fifth power of its size. It is often parametrized in terms of the so-called (tidal) 'Love numbers', e.g. [23, 24], which are analogous to susceptibilities in electrodynamics. These Love numbers modify the phase of the GW signal for inspiraling binary systems at fifth Post-Newtonian (5PN) order [25, 26]. For rapidly rotating bodies, finite-size effects become relevant already at 2PN, through intrinsic spin-induced multipole moments [11, 27, 28]. In either case, the challenge is to extract the parameters of the source accurately [29–31], which requires very precise waveforms.[1] As we shall see, both the Love numbers and the spin-dependent multipoles may carry the imprint of new degrees of freedom. The Love numbers in particular offer a unique diagnostic, since they vanish for BHs in Einstein gravity [23, 24, 49, 50], and therefore any non-zero value would point to physics beyond the Standard Model [7, 21, 22].

New physics may also appear at distances larger than the size of the objects in a binary. This may entail long-distance modifications of General Relativity or extra fields as in scalar-tensor theories. In either case, if the scale of new physics is shorter than the separation between the bodies, decoupling still applies, as far as the computation of GW observables is concerned. For example, modifications of General Relativity can be evidenced during the inspiral phase through higher-derivative corrections to the Einstein-Hilbert action, see e.g. [51]. On the other hand, additional degrees of freedom can have effects at longer distances if their Compton wavelength is

[1] The current state-of-the-art in analytic computations is approaching 4PN order [28, 32–48], moving foward toward the key 5PN threshold [7, 8].

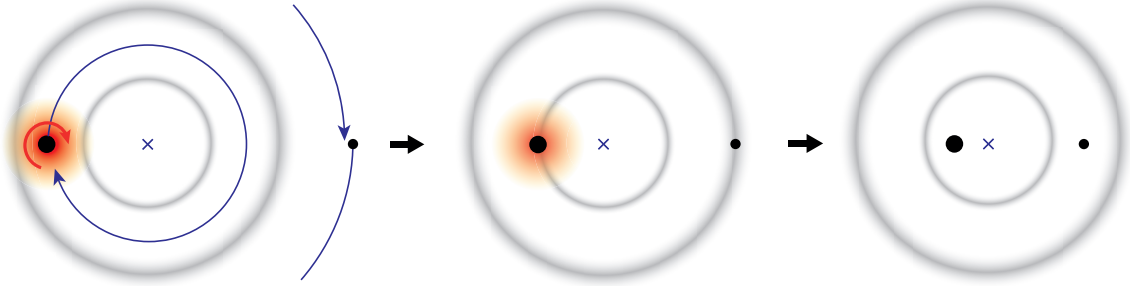

Figure 1: Schematic illustration of the evolution of the boson cloud during the inspiral. The system experiences a resonance when the orbital frequency matches the energy difference between growing and decaying modes. The orbits for which the resonance occurs are indicated by the gray bands, marking the point when the cloud may rapidly deplete leading to novel GW signatures.

larger than the size of the compact objects. This will lead, as we shall see, to larger natural values for the finite-size coefficients in the effective theory, enhanced by powers of the ratio between the Compton scale and gravitational radius. In this manner, new physics may manifest itself at scales larger than anticipated from the Standard Model plus Einstein gravity alone.

A notable example for physics beyond the Standard Model are 'ultralight' particles [52]. Even though the masses for these particles can be many orders of magnitude smaller than those of known elementary particles, they are technically natural if the coupling to ordinary matter is very weak. At the same time, the required weak coupling makes detecting these particles by traditional experimental means extremely challenging. On the other hand, their large Compton wavelengths means that, if present in nature, they will be efficiently produced by the superradiance instability of rapidly rotating BHs [53–59]. For bosonic fields, superradiance creates a classical condensate which can carry a significant amount of the total mass and angular momentum of the system, see [60] for a review. Rather quickly, on cosmological/astrophysical scales, this leads to the BH carrying an 'atmosphere', with a large 'cloud' of the field co-rotating with the BH (see Fig. 1).[2] In the non-relativistic limit, the eigenfunctions of the system are determined by a Schrödinger-like equation and the whole set up is sometimes referred to as a 'gravitational atom'.

The bosons which can be produced in this manner span a vast range of masses, from 10^{-20} to $10^{-10}\,\mathrm{eV}$, corresponding to BHs of a few to billions of solar masses. At the upper end of this range we may find particles which play the role of the QCD axion [61–63], while those at the lower end offer alternative dark matter candidates, both with real [64] and complex [65] scalars. In addition, a plethora of ultralight axion-like particles arise also as a natural consequence of most string compactifications [66, 67]. The 'axiverse' [68], as it is commonly known, includes fields with a wide range of masses, increasing the chances some of them may have formed boson clouds through superradiance instabilities.

[2]These clouds are a form of 'BH hair'. We emphasize, however, that this is not a violation of no-hair theorems for BHs, since these configurations are unstable, eventually returning to the Kerr solution. Nevertheless, if the lifetime is long compared to astrophysical or cosmological timescales, then the BH will carry hair for all practical purposes.

In this paper, we investigate the GW signatures from boson clouds surrounding BHs, when the latter are part of a binary. As we will show, the existence of a companion greatly enriches the dynamical evolution of the entire system. One of the most important consequences of the gravitational perturbation occurs when the orbital frequency of the binary matches the energy difference between growing and decaying modes of the cloud, leading to resonant transitions between the two states. This effect is analogous to Rabi transitions in the hydrogen atom under the influence of an oscillating external field. The resonances can deplete (or significantly attenuate) the energy density stored in the cloud, leading to rich phenomenological implications and powerful new probes of physics beyond the Standard Model.

For real bosonic fields, there are two main sources of GW radiation: *i*) a continuous monochromatic signal from the cloud [69] and *ii*) emission from the two-body system, that includes the BH-cloud system and its companion. The former is absent for complex scalar fields, due to its axisymmetric configuration around the BH. Both signals, when present, will be affected by the dynamical evolution of the cloud in the binary, in particular as the system evolves through the resonances. Notably, the amplitude of the continuous signal emitted from the cloud may be reduced, and in many cases terminated, much before the binary merger. The boson clouds can also reveal themselves through finite-size effects in the GW signal from the binary during the inspiral, such as spin-induced multipole moment(s) and tidal Love number(s). The time-dependence of the cloud during the resonance leads to a sharp feature, or at least an attenuation, in the contribution from finite-size effects to the waveforms. The observation of these phenomenological effects would help us elucidate the nature of the BH-cloud system, and the putative ultralight bosons, through precision GW data.

Using high-precision GW observations to constrain the particle content in the universe resembles the discipline of collider physics. In our case, a scattering process takes place between the rotating BH and an incident wave of the bosonic field. The superradiant amplification of the scattered wave is a type of 'resonance' that occurs when the Compton wavelength of the field exceeds the size of the BH horizon. This resonance creates a large number of ultralight bosons in the intermediate state, which, in the case of real scalars, then decay via self-annihilation into GWs. These GWs can be thought of as many soft quanta in the final state, whose frequency is given by (twice) the mass of the boson. In a binary system, the initial state features an extra body, producing a final state that includes the GWs emitted during the inspiral. The existence of a 'three-body' initial state leads to an additional resonant behavior, opening new decaying channels for the bosonic field. This new configuration enables us to extract more information about the intermediate state. In particular, the coefficients of finite-size terms in the worldline theory carry the imprints of new particles, which, as we will show, can be constrained by GW precision data. This is analogous to precision tests in particle physics, where constraints on the coefficients of higher-dimension operators probe new physics beyond the Standard Model [70].

A similar analogy, between collider physics and the imprints of massive particles in cosmological correlation functions, was drawn in [71].[3] Taking inspiration from cosmology, we will refer

[3] In the case of the 'cosmological collider', particles are produced as 'resonances', when their Compton wavelength exceeds the cosmological horizon during inflation. The properties of the new particles in the intermediate state are reflected in the momentum scaling and angular behavior in the soft limits of correlation functions [71–82].

to this nascent discipline in GW science as 'gravitational collider physics', which complements other searches for new light particles, in the lab [52], astrophysics [83] and cosmology [84–86].

Outline The outline of the paper is as follows: In Section 2, we review how superradiance generates boson clouds around rotating BHs, and compute their energy spectrum. In Section 3, we study the dynamics of the BH-cloud when it is part of a binary. We show that the gravitational perturbation produced by a companion induces resonant mixing between growing and decaying modes of the cloud. We determine the efficiency of this level mixing to deplete the energy density in the cloud, as a function of the parameters of the system. In Section 4, we discuss how the novel features in the dynamics of the BH-cloud affect GW signals, either directly from the cloud or the two-body system including the companion. We estimate the relevant finite-size effects, as well as their time dependence induced by the evolution of the cloud. We then briefly discuss the novel type of constraints on ultralight bosons in binary inspirals, through GW searches both from the cloud and the binary system. We conclude, in Section 5, with a summary of our results and a discussion of open problems. We also provide an outlook on future applications of the gravitational collider. A number of appendices contain additional material: In Appendix A, we derive various properties of the BH-cloud, including the higher-order (hyper)fine structure of its energy spectrum and its quadrupole moment. In Appendix B, we provide an alternative perspective on the absence of a dipole induced by the companion object. Finally, in Appendix C, we review aspects of the EFT approach for extended objects and introduce the relevant finite-size corrections.

Notation and conventions Our metric convention is $(-,+,+,+)$. We will use natural units, $\hbar = c = G = 1$, throughout. The gravitational radius of an object of mass M is $r_g \equiv GM/c^2 = M$. Properties of the boson cloud will be denoted by the subscript c, e.g. M_c and r_c are the mass and typical radius of the cloud. We use the subscript $*$ for quantities related to the companion, e.g. M_* is its mass and V_* is the induced gravitational potential. Ignoring the small energy loss in GW emission, the mass of the BH-cloud is equal to the initial BH mass, and we use M for both of them. We denote by J the initial BH angular momentum, which is also equal to that of the BH-cloud. We define the BH spin parameters $\tilde{a} = a/M = J/M^2$. The mass and spin of the BH at the moment when superradiance saturates are denoted by the subscript s, i.e. M_s and a_s. We introduce the dimensionless variables κ and Λ to describe the spin-induced quadrupole and tidal Love number. For a Kerr BH, we have $\kappa = 1$ and $\Lambda = 0$.

2 Boson Clouds around Black Holes

When a BH rotates faster than the angular phase velocity of an incoming wave, it amplifies the energy and angular momentum of the field in its vicinity.[4] This superradiance effect [53–57] is a natural mechanism to create clouds of ultralight bosons around Kerr BHs (see [60] for a review). In this section, we will review this phenomenon and the properties of the boson clouds that it generates.

2.1 Black Hole Superradiance

Consider a rotating BH of mass M and spin $J \equiv aM$. A bosonic field with mass μ and angular frequency ω experiences a superradiant instability if

$$\frac{\omega}{m} < \Omega_{\rm H} = \frac{a}{2Mr_+}\,, \tag{2.1}$$

where m is the azimutal angular momentum of the field, $\Omega_{\rm H}$ is the angular velocity of the black hole and $r_+ \equiv M + \sqrt{M^2 - a^2}$ is the size of the event horizon of the black hole (see Appendix A). Superradiant growth requires $m > 0$, i.e. modes that co-rotate with the Kerr black hole.

In principle, superradiance occurs for both massive and massless fields. However, the mass of the bosonic field plays the crucial role of a reflecting barrier, so that the superradiantly amplified field is reflected back onto the black hole and continuously extracts angular momentum from it. This provides a natural realization of the 'black-hole bomb' scenario proposed by Teukolsky and Press [88]. The amplitude of the field increases while the black hole spin decreases, until the inequality (2.1) is saturated. The black hole spin at saturation is

$$\frac{a_s}{M_s} = \frac{4m(M_s\omega_s)}{m^2 + 4(M_s\omega_s)^2}\,, \tag{2.2}$$

where M_s and ω_s are the relevant quantities evaluated after superradiance has ended. The existence of black holes with spins above this critical value would rule out ultralight scalar fields in the corresponding mass range [69].

Although superradiance is a phenomenon that occurs for bosons of any spin [56, 57, 89], in the rest of the paper we will focus only on the scalar case. The reason is twofold: from a practical point of view, the Klein-Gordon equation for a massive scalar field in a Kerr background is separable in Boyer-Lindquist coordinates [90, 91], which makes the problem analytically tractable (see Appendix A). This is not the case for massive vector and tensor fields. From a theoretical point of view, ultralight scalar fields arise naturally as particle candidates in various scenarios for physics beyond the Standard Model. The Kerr-scalar system is therefore a particularly well-motivated system to be studied.

2.2 Gravitational Atom

The equation of motion of a massive scalar field Ψ around a rotating BH is

$$\left(g^{ab}\nabla_a\nabla_b - \mu^2\right)\Psi(t,\mathbf{r}) = 0\,, \tag{2.3}$$

[4] This is the rotational analogue of Cherenkov radiation [87], where spontaneous emission of light occurs when a test particle moves with a speed that is faster than the phase velocity of the medium.

where g_{ab} is the Kerr metric and ∇_a is the associated covariant derivative. To study the dynamical evolution of Ψ in the non-relativistic limit, it is convenient to consider the ansatz

$$\Psi(t,\mathbf{r}) = \begin{cases} \dfrac{1}{\sqrt{2\mu}}\left[\psi(t,\mathbf{r})\, e^{-i\mu t} + \psi^*(t,\mathbf{r})\, e^{+i\mu t}\right] & \Psi \text{ real}\,, \\ \dfrac{1}{\sqrt{2\mu}}\,\psi(t,\mathbf{r})\, e^{-i\mu t} & \Psi \text{ complex}\,, \end{cases} \tag{2.4}$$

where $\psi(t,\mathbf{r})$ is a complex scalar field which varies on a timescale that is much longer than μ^{-1}. Substituting (2.4) into (2.3), and keeping only the leading contributions in r^{-1}, the field $\psi(t,\mathbf{r})$ satisfies the Schrödinger equation with a Coulomb-like central potential

$$i\frac{\partial}{\partial t}\psi(t,\mathbf{r}) = \left[-\frac{1}{2\mu}\nabla^2 - \frac{\alpha}{r}\right]\psi(t,\mathbf{r})\,, \tag{2.5}$$

where we have defined the 'fine-structure constant'

$$\alpha \equiv \frac{GM\mu}{\hbar c} \simeq 0.02\left(\frac{M}{3M_\odot}\right)\left(\frac{\mu}{10^{-12}\,\mathrm{eV}}\right). \tag{2.6}$$

Notice that α is the ratio of the gravitational radius of the BH, $r_g \equiv GM/c^2$, and the (reduced) Compton wavelength of the scalar field, $\lambda_c \equiv \hbar/(\mu c)$.

Energy spectrum

Remarkably, the Schrödinger equation (2.5) takes the same form as for the hydrogen atom, such that the stationary eigenstates $\psi_{n\ell m}$ around the BH are given by the hydrogenic eigenfunctions (see Appendix A for details)

$$\psi_{n\ell m}(t,\mathbf{r}) \simeq e^{-i(\omega-\mu)t}\bar{R}_{n\ell}(r)Y_{\ell m}(\theta,\phi)\,, \tag{2.7}$$

where $\{n,\ell,m\}$ are the principal, orbital, and magnetic 'quantum numbers' respectively, which satisfy $\ell \leq n-1$ and $|m| \leq \ell$. For future convenience, we denote these eigenstates by $\psi_{n\ell m} \equiv |n\ell m\rangle$, and refer the occupied states as 'clouds'. The eigenfrequencies are given by

$$\omega_{n\ell m} \simeq \mu\left(1 - \frac{\alpha^2}{2n^2}\right). \tag{2.8}$$

The radial profile of the scalar cloud peaks at

$$r_c \simeq \left(\frac{4}{\alpha^2}\right) r_g\,, \tag{2.9}$$

which can be far away from the central BH for $\alpha \ll 1$.

Fine structure and beyond

Keeping higher powers of r^{-1} in the large distance expansion, one obtains higher-order corrections to the eigenfrequencies (2.8) (see Appendix A for details):

$$\Delta\omega_{n\ell m} = \mu\left(-\frac{\alpha^4}{8n^4} + \frac{(2\ell-3n+1)\,\alpha^4}{n^4(\ell+1/2)} + \frac{2\tilde{a}m\alpha^5}{n^3\ell(\ell+1/2)(\ell+1)}\right). \tag{2.10}$$

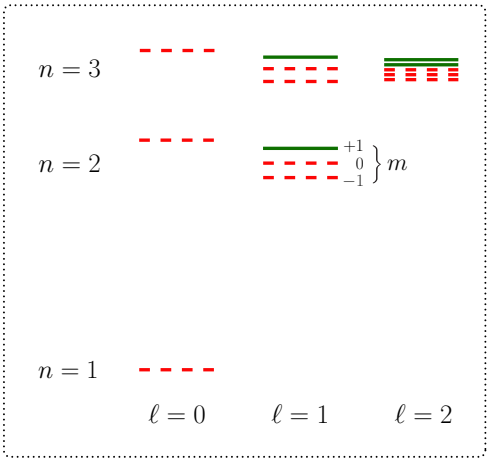

Figure 2: Illustration of the eigenfrequency spectrum of the cloud, up to $n = 3$ and $\ell = 2$. Green (solid) lines represent growing modes, while the red (dashed) lines are decaying modes. For a given value of n and ℓ, the lowest frequency level is the $m = -\ell$ mode, and subsequent higher frequencies are levels with larger values of m.

The individual terms in (2.10) are analogous to the relativistic correction to the kinetic energy, the fine splitting ($\Delta\ell \neq 0$) and the hyperfine splitting ($\Delta m \neq 0$) in the hydrogen atom. These corrections break the degeneracies between modes of the same n but different ℓ and m (see Fig. 2). As we shall see in Section 3, the presence of an external perturbation can induce transitions between these energy levels.

Decay width

The analogy between the gravitational atom and the hydrogen atom is of course not exact. An obvious distinction is that electrons in the hydrogen atom are fermions, while the cloud is bosonic. This means that each level of the gravitational atom can be occupied by an exponentially large number of scalar quanta [69], forming a boson *condensate*. Moreover, the states are not perfectly stationary, due to the boundary conditions at the horizon. This is encapsulated in the imaginary part of the eigenfrequency,

$$\omega_{n\ell m} \to \omega_{n\ell m} + i\Gamma_{n\ell m}\,, \tag{2.11}$$

which was omitted in (2.8). In general, the instability rate has to be determined numerically [92]. However, in the limit $\alpha \ll 1$, the decay width can be computed analytically. The result, known as 'Detweiler's approximation', is given by [93]

$$\Gamma_{n\ell m} = \frac{2r_+}{M} C_{n\ell m}(\alpha)\,(m\Omega_{\rm H} - \omega)\,\alpha^{4\ell+5}\,, \tag{2.12}$$

where we defined[5]

$$C_{n\ell m}\,(\alpha) \equiv \frac{2^{4\ell+1}(n+\ell)!}{n^{2\ell+4}(n-\ell-1)!}\left[\frac{\ell!}{(2\ell)!(2\ell+1)!}\right]^2 \prod_{j=1}^{\ell}\left[j^2\left(1-\tilde{a}^2\right) + \left(\tilde{a}m - 2\tilde{r}_+\alpha\right)^2\right], \tag{2.13}$$

[5]See also the appendix of [94], which points out a missing factor of 1/2 in Detweiler's original computation.

with $\tilde{a} \equiv a/M$ and $\tilde{r}_+ \equiv r_+/M$. Although the analytic result (2.12) was obtained for $\alpha \ll 1$, it was found to give reasonable agreements with numerical results for $\alpha < 0.5$ (see Fig. 28 in [60]).

Due to the strong dependence of Γ on ℓ, the dominant growing modes have $\ell_g = m_g = 1$. In principle, this includes an infinite tower of overtones $|n_g 11\rangle$, with $n_g \geq 3$, but, in practice, the fastest growing mode is $|211\rangle$. Moreover, at the end of the superradiant growth, we have $\omega_{n_g 11} > \omega_{211} = \Omega_{\rm H}$, so that the higher overtones decay back into the black hole. Hence, in the rest of the paper, we will consider $|211\rangle$ as the initial condition. The observationally relevant range of α is then given by

$$0.005 \left(\frac{M}{3M_\odot}\right)^{1/9} \lesssim \alpha < 0.5\,, \tag{2.14}$$

where the lower bound is obtained by demanding the cloud to grow significantly within the age of the universe, while the upper bound is the maximum value of α for superradiant growth of the $|211\rangle$ mode to occur, assuming an initial BH spin of $\tilde{a} = 0.99$. Smaller values of $\tilde{a}$ result in stronger upper bounds on α. For instance, $\tilde{a} = 0.8$ implies $\alpha < 0.25$ [92].

2.3 Continuous Emission

While the energy spectra of real and complex boson clouds are identical, their stability properties are very different. In particular, complex scalar fields do not induce time-dependent perturbations of the background metric, and therefore do not source GWs. The energy-momentum tensor of a real scalar field, on the other hand, is time dependent, as well as non-axisymmetric. As a consequence, clouds made out of real scalars are a continuous source of GWs [69]. Since the timescale for this GW emission is much longer than the timescale of the superradiance instability, it doesn't inhibit the formation of the clouds [95]. However, depending on the values of M and α, the clouds may still deplete on cosmological/astrophysical timescales.

The rate of GW emission for a real scalar cloud is given by[6]

$$\frac{dE_{\rm gw}}{dt} \simeq 0.01 \left(\frac{M_c(\alpha)}{M}\right)^2 \alpha^{14}\,, \tag{2.15}$$

where the numerical coefficient was obtained from a fit to the numerical results of [95, 96] and $M_c(\alpha)$ is the mass of the cloud as a function of α. For $\alpha \ll 1$, and assuming the initial BH spin to be close to maximal, $\tilde{a} \to 1$, we can approximate $M_c(\alpha) \simeq M\alpha$ [96].[7] In the absence of additional effects such as accretion disks, conservation of energy implies $\dot{M}_c = -\dot{E}_{\rm gw}$, and the cloud evolves as

$$M_c(t) = \frac{M_{c,0}}{1 + t/\tau_c}\,, \tag{2.16}$$

[6] Comparison with numerical results [95, 96] suggests that (2.15) is a good approximation for $\alpha \lesssim 0.1$. For larger values of α, nonlinear effects reduce the emission power, and (2.15) is only an upper bound.

[7] For larger values of α, determining $M_c(\alpha)$ requires numerical simulations; see [58] for the extraction efficiencies for complex Proca fields in near extremal BH backgrounds. The theoretical upper limit of superradiance extraction is given by $M_c/M < 0.29$ [97].

where $M_{c,0}$ is the initial mass of the cloud and τ_c the lifetime of the cloud, which is given by

$$\begin{aligned} \tau_c &\simeq 10^7 \text{ years} \left(\frac{M}{3M_\odot}\right)\left(\frac{0.07}{\alpha}\right)^{15}, \\ &\simeq 10^9 \text{ years} \left(\frac{M}{10^5 M_\odot}\right)\left(\frac{0.1}{\alpha}\right)^{15}. \end{aligned} \tag{2.17}$$

These estimates are valid for $\alpha \lesssim 0.1$, while for larger values of α, (2.17) can underestimate τ_c up to two orders of magnitude (see footnote 6).

We see that the cloud's lifetime is extremely sensitive to the value of α. For stellar-mass BHs, with masses in the range $[3, 100]\, M_\odot$, we can ignore the GW emission from the cloud for typical binary dynamical timescales of order 10 Myr to 1 Gyr (e.g. [98] and references therein), provided that $\alpha \lesssim 0.07$. On the other hand, for supermassive BHs with $M \gtrsim 10^5 M_\odot$, the cloud survives for more than 1 Gyr if $\alpha \lesssim 0.1$. If the BHs continuously accrete matter, long-lived clouds may be allowed with larger values of α [99]. The associated ranges of α will become relevant when we discuss the evolution of the BH-cloud in a binary system, and in particular its GW signatures. While GW emission from the cloud may be ignored for evolution timescales that are smaller than τ_c, other depletion channels may become active in the presence of a companion. We will discuss this next.

3 Clouds in Binary Systems

So far, we have studied the BH-cloud in isolation, where it can be described by quasi-stationary states. As we shall see, these configurations are altered when the BH carrying the cloud is part of a binary system (with a companion which may or may not carry a cloud itself). We will find that the gravitational perturbations on the BH-cloud yield interesting new phenomena. In particular, we will discover the presence of resonant orbital frequencies for the binary, which lead to new instabilities for the BH-cloud. We will discuss the observational consequences of these resonances in Section 4.

3.1 Gravitational Perturbations

The presence of a companion, of mass M_*, introduces a perturbation to the dynamics of the cloud. We will concentrate on the gravitational potential in the free-falling frame of the cloud, but also briefly discuss the possibility of mass/energy transfer between the cloud and the companion. As long as the binary separation, R_*, is larger than the size of the cloud, $R_* > r_c$, the gravitational influence of the companion can be treated in a multipole expansion. Furthermore, we will assume that the correction to the Kerr metric is a small perturbation. This requires the length scale associated to the gravitational (curvature) perturbation $\sqrt{R_*^3/M_*}$ to be larger than r_c, or equivalently $R_* > 2^{-2/3} q^{1/3} \alpha^{2/3} r_c$, where $q \equiv M_*/M$. For $\alpha < 1$, the latter condition is somewhat weaker than the requirement of negligible mass transfer (see below), which reads $R_* > 2q^{1/3} r_c$. Taking this into account, the regime of validity of our perturbative treatment is bounded by $R_* > R_{\rm pt} \equiv \max\{r_c, 2q^{1/3} r_c\}$.

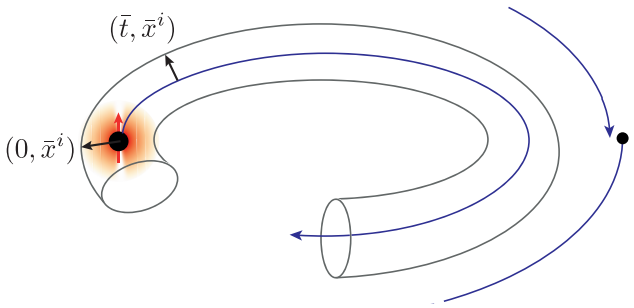

Figure 3: Fermi coordinates $(\bar{t}, \bar{x}^i)$ centered on the geodesic of the BH-cloud system.

Free-falling clouds

The perturbed metrics for BHs in external fields have been studied extensively in the literature, see e.g. [100] and references therein. The companion object induces a time-dependent perturbation to the metric, such that $g_{\mu\nu} = g^{(0)}_{\mu\nu} + \delta g_{\mu\nu}$, where $g^{(0)}_{\mu\nu}$ is the unperturbed Kerr spacetime. In general, the metric perturbation $\delta g_{\mu\nu}$ consists of two separate components: *i*) a direct contribution from the gravitational potential due to M_*, and *ii*) the response of the BH-cloud to tidal deformations. We will work in the Newtonian limit, which dominates the gravitational perturbation to the cloud due to the companion, and ignore the subleading tidal contributions, as well as the effect of the BH spin on the metric. (We will discuss tidal and spin-induced effects in §4.2, when we study the GW signal from the binary system.)

In comoving Fermi coordinates $(\bar{t}, \bar{x}^i)$, whose origin is located at the centre-of-mass[8] of the unperturbed BH-cloud (see Fig. 3), the δg_{00} component reads [100, 101]

$$\begin{aligned} \delta g_{00}(\bar{t}, \bar{r}) &= \sum_{\ell_*=2} \frac{2}{\ell_*(\ell_*-1)} \mathcal{E}_L(\bar{t}, 0)\, \bar{x}^L \\ &= \sum_{\ell_*=2} \sum_{|m_*|\leq \ell_*} \frac{2}{\ell_*(\ell_*-1)} \bar{r}^{\ell_*}\, \mathcal{E}^{(m_*)}_{\ell_*}(\bar{t}, 0)\, Y_{\ell_* m_*}(\bar{\theta}, \bar{\phi})\,, \end{aligned} \tag{3.1}$$

where we have used the notation $L \equiv (i_1 \cdots i_{\ell_*})$. The tensor $\mathcal{E}_L$ is the symmetric trace-free representation of the tidal tensor, defined as $\mathcal{E}_L(\bar{t}, 0) \equiv -\partial_L U_*(\bar{t}, 0)/(\ell_* - 2)!$, with $U_*(\bar{t}) = -M_*/R_*(\bar{t})$ the gravitational potential generated by the companion, evaluated along the geodesic of the BH-cloud. In the second line of (3.1) we have decomposed the gravitational field into spherical harmonics in polar coordinates $\bar{\mathbf{r}} \equiv \{\bar{r}, \bar{\theta}, \bar{\phi}\}$, with coefficients $\mathcal{E}^{(m_*)}_{\ell_*}(\bar{t}, 0)$. The fact that the expansion (3.1) in the *free-falling* frame begins with two derivatives of the external potential is a well-known consequence of the equivalence principle.

The tidal tensors can easily be computed. For example, at leading Newtonian order, the $\ell_* = 2$

[8] In our case, the center-of-mass of the BH-cloud coincides with that of the isolated BH, such that the $(\bar{t}, \bar{x}^i)$ coordinates may be directly related to the Boyer-Lindquist coordinates of the Kerr metric.

mode is [102]

$$\begin{aligned}\mathcal{E}_{ij}(t,0)\,\bar{x}^i\bar{x}^j &= -\frac{3M_*}{R_*^3}\left(\hat{n}_i\hat{n}_j-\frac{1}{3}\delta_{ij}\right)\bar{x}^i\bar{x}^j \\ &= -\frac{8\pi}{5}\frac{M_*}{R_*}\left(\frac{\bar{r}}{R_*}\right)^2\sum_{m_*=-2}^{2}Y^*_{2m_*}(\Theta_*,\Phi_*)Y_{2m_*}(\bar{\theta},\bar{\phi})\,,\end{aligned} \tag{3.2}$$

where $\mathbf{R}_*(t)\equiv\{R_*(t),\Theta_*(t),\Phi_*(t)\}$ describes the position of the companion relative to the BH-cloud frame, $\hat{\mathbf{n}}\equiv\mathbf{R}_*/|\mathbf{R}_*|$, and t now corresponds to the time measured by asymptotic observers, as opposed to observers in the free-falling frame.[9] At this order, we thus have

$$\mathcal{E}^{(m_*)}_{\ell_*=2}(t,0)=-\frac{8\pi}{5}\frac{M_*}{R_*^3}Y^*_{2m_*}(\Theta_*,\Phi_*)\,. \tag{3.3}$$

Using these results, and considering higher harmonics, it is straightforward to find the corrected gravitational dynamics in the non-relativistic limit. Substituting the perturbed metric into the Klein-Gordon equation, we find that, at lowest order, the gravitational potential in the Schrödinger-like equation (2.5) is simply shifted by

$$V_*(t,\bar{r})\;=\;\frac{1}{2}\mu\,\delta g_{00}\;=\;-\frac{M_*\mu}{R_*}\sum_{\ell_*\geq 2}\sum_{|m_*|\leq\ell_*}\frac{4\pi}{2\ell_*+1}\left(\frac{\bar{r}}{R_*}\right)^{\ell_*}Y^*_{\ell_*m_*}(\Theta_*,\Phi_*)\,Y_{\ell_*m_*}(\bar{\theta},\bar{\phi})\;. \tag{3.4}$$

Crucially, the first contribution starts with the *quadrupole* $\ell_*=2$. In principle, a different choice of observers/coordinates — not free-falling with the BH-cloud — could lead to the appearance of extra terms in the potential, for instance a *dipole*. However, as we show in Appendix B, this fictitious dipole eventually cancels. Finally, the above reasoning can be generalized to incorporate all types of relativistic corrections.

In summary, the Klein-Gordon equation for the BH-cloud system receives corrections due to the presence of a companion which, in the non-relativistic limit, lead to a perturbed gravitational potential (3.4). The salient feature is the fact that the multipolar interaction starts at the quadrupole level, as determined by the equivalence principle.

Mass transfer

The mutual gravitational attraction between the bodies can also induce transfer of mass/energy between the cloud and the companion. This happens when the characteristic Bohr radius r_c exceeds the Lagrange point, $L1$, located in between the two objects of the binary. The equipotential surface with the same gravitational potential as $L1$ is called the Roche lobe (see Fig. 4).

Mass transfer from the cloud to the companion happens when $r_c\gtrsim R_{\rm Roche}$. Using Eggleton's fitting formula [103], this can be converted into a critical orbital separation

$$R_{*,\rm cr}\equiv\left(\frac{0.49\,q^{-2/3}}{0.6\,q^{-2/3}+\ln\left(1+q^{-1/3}\right)}\right)^{-1}r_c\,. \tag{3.5}$$

[9] The distinction between time coordinates only plays a role at higher post-Newtonian orders, e.g. [100], when the boost factors begin to contribute.

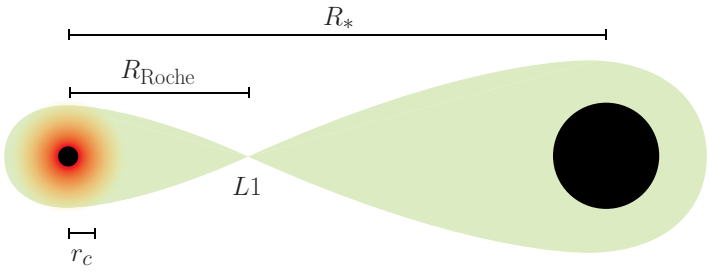

Figure 4: Illustration of the Roche lobes for a binary with $q \gg 1$. As the separation decreases, the Roche lobe of the BH-cloud begins to shrink. At the critical value $R_{*,\rm cr}$, given by (3.5), the size of the cloud r_c exceeds $R_{\rm Roche}$, and mass transfer starts to occur.

This phenomenon becomes particularly important when $q \gg 1$, since the Roche lobe surrounding the BH carrying the cloud is then relatively small. In this limit, we find

$$R_{*,\rm cr} \simeq 2q^{1/3} r_c \,. \tag{3.6}$$

In the rest of the paper, we will impose $R_* > R_{*,\rm cr}$, such that mass transfer can be ignored.

3.2 Level Mixing

The gravitational perturbation V_* in (3.4) induces an overlap between the modes $|\psi_i\rangle \equiv |n_i \ell_i m_i\rangle$ and $|\psi_j\rangle \equiv |n_j \ell_j m_j\rangle$, through $\langle \psi_j | \, V_* \, |\psi_i\rangle$. Substituting (3.4), we get

$$\langle \psi_j | \, V_* \, |\psi_i\rangle = -M_* \mu \sum_{\ell_* \geq 2} \sum_{|m_*| \leq \ell_*} \frac{4\pi}{2\ell_* + 1} \frac{Y^*_{\ell_* m_*}(\Theta_*, \Phi_*)}{R_*^{\ell_*+1}} \times I_{\bar{r}} \times I_\Omega \,, \tag{3.7}$$

where

$$I_{\bar{r}} \equiv \int_0^\infty \mathrm{d}\bar{r}\, \bar{r}^{2+\ell_*} \bar{R}_{n_j \ell_j}(\bar{r}) \bar{R}_{n_i \ell_i}(\bar{r}) \,, \tag{3.8}$$

$$I_\Omega \equiv \int \mathrm{d}\Omega \; Y^*_{\ell_j m_j}(\bar{\theta}, \bar{\phi})\, Y_{\ell_i m_i}(\bar{\theta}, \bar{\phi})\, Y_{\ell_* m_*}(\bar{\theta}, \bar{\phi}) \,. \tag{3.9}$$

The angular integral I_Ω can be expressed in terms of the Wigner 3-j symbol,

$$I_\Omega = \sqrt{\frac{(2\ell_j+1)(2\ell_i+1)(2\ell_*+1)}{4\pi}} \begin{pmatrix} \ell_j & \ell_i & \ell_* \\ 0 & 0 & 0 \end{pmatrix} \begin{pmatrix} \ell_j & \ell_i & \ell_* \\ -m_j & m_i & m_* \end{pmatrix} , \tag{3.10}$$

which implies the following *selection rules*:

(S1) $-m_j + m_i + m_* = 0 \,,$

(S2) $|\ell_j - \ell_i| \leq \ell_* \leq \ell_i + \ell_j \,,$

(S3) $\ell_i + \ell_j + \ell_* = 2p$, for $p \in \mathbb{Z} \,.$

Recall that the fastest growing mode $|211\rangle$ has $\ell_g = m_g = 1$, while the fastest decaying mode $|100\rangle$ has $\ell_d = m_d = 0$. In this case, the above selection rules would require $\ell_* = \pm m_* = 1$, namely a *dipole* coupling, which is absent in (3.4). For the quadrupole, the two fastest decaying modes that can couple to $\ell_g = m_g = 1$ are $\ell_d = 1, m_d = -1$ and $\ell_d = 1, m_d = 0$. Since these rules are obtained purely from the angular dependence of the eigenfunctions, they apply equally to the fundamental mode ($n = 2$) and the overtones ($n \geq 3$).

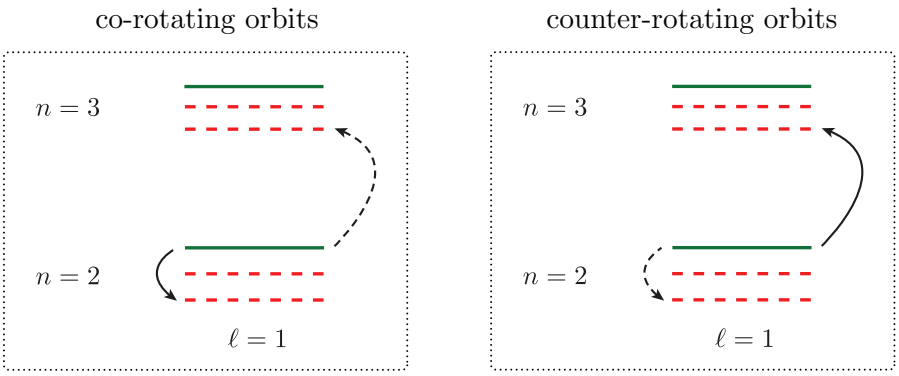

Figure 5: Illustration of the frequency spectrum for $\ell = 1$ up to $n = 3$ (there is in principle an infinite tower of overtones), for co-rotating and counter-rotating orbits. Solid arrows represent the allowed resonant transitions, while dashed arrows denote perturbative level mixings.

3.3 Rabi Resonances

We now investigate how level mixings (see Fig. 5), induced by the quadrupole $\ell_* = 2$, affect the dynamical evolution of the cloud. For simplicity, we will restrict ourselves to quasi-circular orbits with orbital frequency

$$\Omega \equiv \sqrt{\frac{M + M_*}{R_*^3}}\,, \tag{3.11}$$

where M is the total mass of the BH-cloud, which is equal to the initial BH mass *before* superradiance, if we neglect the small mass loss due to GW emission. Since Φ_* denotes the azimuthal angle of M_* relative to the BH-cloud, the orientation $\Phi_* = +\Omega t$, with $\Omega > 0$, corresponds to orbits that co-rotate with the cloud, called *co-rotating* orbits, while $\Phi_* = -\Omega t$ are *counter-rotating* orbits. This distinction will play a key role in the survival of the cloud throughout the inspiral stage. For notational convenience, we will write $\Phi_* = \pm\Omega t$, where the upper sign corresponds to co-rotating orbits and the lower sign denotes counter-rotating orbits.

3.3.1 Hyperfine Mixing

We first consider the mixing of the dominant growing mode $|211\rangle$ with the nearby decaying modes $|210\rangle$ and $|21-1\rangle$. The problem then involves the dynamics of a coupled three-state system. As we shall see, for orbital motions along the equatorial plane, the mode $|210\rangle$ decouples and the dynamics reduces to a two-state system.

Three-state system

For the three-state system, the expectation value of Hamiltonian for the field ψ takes the form

$$H = H_0 + H_1 + H_2\,, \tag{3.12}$$

where H_0 represents the diagonal terms that contribute equally to all three modes, H_1 contains terms that split the degeneracy, and H_2 are the off-diagonal terms induced by the quadrupole

perturbation $\ell_* = 2$. Using the basis $|211\rangle = (1,0,0)^{\mathrm{T}}, |210\rangle = (0,1,0)^{\mathrm{T}}$ and $|21-1\rangle = (0,0,1)^{\mathrm{T}}$, the explicit matrix representations of the different contributions are

$$
\begin{aligned}
H_0 &= \begin{pmatrix} E & 0 & 0 \\ 0 & E & 0 \\ 0 & 0 & E \end{pmatrix}, \qquad H_1 = \begin{pmatrix} \epsilon_h + 3\eta f_0(\Theta_*) & 0 & 0 \\ 0 & -6\eta f_0(\Theta_*) & 0 \\ 0 & 0 & -\epsilon_h + 3\eta f_0(\Theta_*) \end{pmatrix}, \\
H_2 &= \begin{pmatrix} 0 & 3\eta f_1(\Theta_*) e^{\mp i\Omega t} & 3\eta f_2(\Theta_*) e^{\mp 2i\Omega t} \\ 3\eta f_1(\Theta_*) e^{\pm i\Omega t} & 0 & -3\eta f_1(\Theta_*) e^{\mp i\Omega t} \\ 3\eta f_2(\Theta_*) e^{\pm 2i\Omega t} & -3\eta f_1(\Theta_*) e^{\pm i\Omega t} & 0 \end{pmatrix},
\end{aligned}
\tag{3.13}
$$

where we have introduced the following quantities (see Appendix A)

$$
E \equiv \mu \left(-\frac{1}{8}\alpha^2 - \frac{17}{128}\alpha^4 \right), \tag{3.14}
$$

$$
\epsilon_h \equiv \frac{\mu}{12}\, \tilde{a}\, \alpha^5, \tag{3.15}
$$

$$
\eta \equiv \alpha^{-3} \left(\frac{q}{R_*} \right) \left(\frac{r_g}{R_*} \right)^2. \tag{3.16}
$$

The parameter $\epsilon_h > 0$ is the hyperfine splitting, and η characterized the strength of the perturbation, proportional to the expectation value $\langle \psi_j | \, V_* \, | \psi_i \rangle$ given by (3.7) (with $i, j = 1, 2, 3$). The oscillatory terms in H_2 are due to the phase evolution $\Phi_* = \pm \Omega t$. The functions $f_{|m_*|}(\Theta_*)$ arise from the angular dependence of the $\ell_* = 2, m_* = 0, \pm 1$ and ± 2 modes:

$$
\begin{aligned}
f_0(\Theta_*) &\equiv 3\cos^2\Theta_* - 1\,, \\
f_1(\Theta_*) &\equiv 3\sqrt{2}\cos\Theta_* \sin\Theta_*\,, \\
f_2(\Theta_*) &\equiv 3\sin^2\Theta_*\,.
\end{aligned}
\tag{3.17}
$$

For the special case $\Theta_* = \pi/2$ (i.e. equatorial motion), this reduces to $f_0 = -1, f_1 = 0, f_2 = 3$.

It is convenient to work in the interaction picture, where the evolution of the state $|\psi_I\rangle$ is given by

$$
|\psi_I(t)\rangle = e^{iH_I t} \, |\psi(t)\rangle\,, \tag{3.18}
$$

where $H_I \equiv H_0 + H_1$ is time-independent.[10] Since H_I is diagonal, it does not couple modes of different angular momenta. The eigenstates of H_I are therefore equal to the corresponding eigenstates of the non-relativistic hydrogen atom, with the same ℓ and m, up to $\mathcal{O}(\alpha^2)$ corrections which will not be relevant in our case.

Two-state system

We now consider quasi-circular orbits along the equator, where $f_1 = 0$. This reduces the problem to a coupled two-state system, which can be solved *exactly*. Labelling the growing and decaying

[10] Strictly speaking, H_I has a time dependence due to the decrease of the orbital radius $R_*(t)$ in the binary. However, since $\dot{R}_*/R_* \ll \Omega$ during the inspiral stage, this time dependence can be treated adiabatically, and neglected at leading order.

modes as $|\psi_g\rangle \equiv |211\rangle$ and $|\psi_d^{(h)}\rangle \equiv |21-1\rangle$, the state in the interaction picture is expressed as a linear combination

$$|\psi_I(t)\rangle = c_g(t)\,|\psi_g\rangle + c_d^{(h)}(t)\,|\psi_d^{(h)}\rangle\,, \tag{3.19}$$

where the time-dependent coefficients satisfy

$$|c_g(t)|^2 + |c_d^{(h)}(t)|^2 = 1\,. \tag{3.20}$$

The Schrödinger equation becomes

$$i\frac{d}{dt}\begin{pmatrix} c_g(t) \\ c_d^{(h)}(t)\end{pmatrix} = \begin{pmatrix} 0 & 9\eta\, e^{-2i(\pm\Omega-\epsilon_h)t} \\ 9\eta\, e^{+2i(\pm\Omega-\epsilon_h)t} & 0\end{pmatrix}\begin{pmatrix} c_g(t) \\ c_d^{(h)}(t)\end{pmatrix}. \tag{3.21}$$

Starting the evolution in the growing mode, $c_g(0)=1, c_d^{(h)}(0)=0$, we find

$$c_g(t) = \frac{e^{i(\epsilon_h\mp\Omega)t}}{2\Delta_R^{(h)}}\left[\left(\Delta_R^{(h)}+\epsilon_h\mp\Omega\right)e^{-i\Delta_R^{(h)}t} + \left(\Delta_R^{(h)}-\epsilon_h\pm\Omega\right)e^{+i\Delta_R^{(h)}t}\right], \tag{3.22}$$

$$c_d^{(h)}(t) = \frac{9\eta\, e^{-i(\epsilon_h\mp\Omega)t}}{2\Delta_R^{(h)}}\left[e^{-i\Delta_R^{(h)}t} - e^{+i\Delta_R^{(h)}t}\right], \tag{3.23}$$

where we introduced

$$\Delta_R^{(h)} \equiv \sqrt{(9\eta)^2 + (\epsilon_h\mp\Omega)^2}\,. \tag{3.24}$$

Since ψ is a complex scalar field with a global $U(1)$ symmetry, there is an associated conserved Noether current J^μ (see Appendix A for details). At leading order, $J^0 \simeq \psi^*\psi$, which is interpreted as the occupation density of the system, and is analogous to the probability density in quantum mechanics. The occupation density of the decaying mode is proportional to

$$|c_d^{(h)}(t)|^2 = \left[1-\left(\frac{\epsilon_h\mp\Omega}{\Delta_R^{(h)}}\right)^2\right]\sin^2\left[\int_{t_0}^{t}\mathrm{d}t'\,\Delta_R^{(h)}(t')\right]. \tag{3.25}$$

Note that $\Delta_R^{(h)}$ is not constant during the inspiral, but increases as the orbit shrinks, so that the phase of the oscillations in (3.25) has been written as an integral over time. We see that $2\Delta_R^{(h)}$ controls the frequency of oscillations between the growing and decaying modes. In analogy with the quantum mechanical problem, we call this the *Rabi frequency*.

Hyperfine resonance

When the orbital frequency Ω matches the hyperfine splitting ϵ_h, the system experiences a resonance, and starts to oscillate between the growing and decaying modes. Since $\epsilon_h > 0$, the resonance will only take place for co-rotating orbits. We will refer to this effect as the *hyperfine resonance*. This happens when the binary separation is

$$\begin{aligned} R_{\rm res}^{(h)} &= 144^{1/3}\,\alpha^{-4}(1+q)^{1/3}\,\tilde{a}^{-2/3}\,r_g\,, \\ &\simeq 9^{1/3}\,\alpha^{-14/3}\left(1+4\alpha^2\right)^{2/3}(1+q)^{1/3}\left(\frac{a_s}{a}\right)^{2/3} r_g\,, \end{aligned} \tag{3.26}$$

where we have used (2.2) for a_s, with $M_s \simeq M$ and $M_s\omega_s \simeq \alpha$.

3.3.2 Bohr Mixing

We now consider the possibility that the dominant growing mode $|211\rangle$ mixes also with the decaying modes $|n10\rangle$ and $|n1-1\rangle$, with $n \geq 3$. We will take the coupling to the $n=3$ modes to be a proxy for the mixing with this infinite tower of overtones. Similar conclusions hold for the higher-order overtones ($n \geq 4$). In particular, since $\omega_{n1-1} > \omega_{31-1}$, the only difference is that these resonant mixings occur at orbital separations that are slightly shorter. As before, we restrict ourselves to motion in the equatorial plane, $\Theta_* = \pi/2$, so that the $|310\rangle$ mode decouples.

Three-level system

Labelling $|\psi_g\rangle \equiv |211\rangle$ and $|\psi_d^{(h)}\rangle \equiv |21-1\rangle$ as before, but adding the extra decaying mode $|\psi_d^{(b)}\rangle \equiv |31-1\rangle$, the state of the system in the interaction picture is now expressed as the following linear combination

$$|\psi_I(t)\rangle = c_g(t)\,|\psi_g\rangle + c_d^{(h)}(t)\,|\psi_d^{(h)}\rangle + c_d^{(b)}(t)\,|\psi_d^{(b)}\rangle\ , \tag{3.27}$$

with the normalization condition given by

$$|c_g|^2 + |c_d^{(h)}|^2 + |c_d^{(b)}|^2 = 1\,. \tag{3.28}$$

The Schrödinger equation implies

$$i\frac{d}{dt}\begin{pmatrix} c_g(t) \\ c_d^{(h)}(t) \\ c_d^{(b)}(t) \end{pmatrix} = \begin{pmatrix} 0 & 9\eta\, e^{-2i(\pm\Omega-\epsilon_h)t} & -7.6\eta\, e^{-2i(\pm\Omega-\epsilon_b)t} \\ 9\eta\, e^{+2i(\pm\Omega-\epsilon_h)t} & 0 & 0 \\ -7.6\eta\, e^{+2i(\pm\Omega-\epsilon_b)t} & 0 & 0 \end{pmatrix}\begin{pmatrix} c_g(t) \\ c_d^{(h)}(t) \\ c_d^{(b)}(t) \end{pmatrix}, \tag{3.29}$$

with

$$\epsilon_b \equiv -\frac{5}{144}\,\mu\,\alpha^2\,. \tag{3.30}$$

In general, there is no analytic solution for the three-level system (3.29). However, since we have $\epsilon_h/|\epsilon_b| \simeq \alpha^3 \ll 1$, there is a clear hierarchy of scales in the evolution equation, and the system will probe different decaying modes at different times. The strength of the coupling — away from resonances — is determined by the ratio of the size of the gravitational perturbation to the energy split. During the early stages of the inspiral, when $\Omega \lesssim |\epsilon_h|$, the mixing with the hyperfine state dominates. The solutions for $c_g(t)$ and $c_d^{(h)}(t)$ are thus identical to those given in (3.25), with an error in the normalization condition of order $(\epsilon_h/\epsilon_b)^2$. As we have seen, for co-rotating orbits, the binary experiences a resonance when $\Omega = \epsilon_h$, while counter-rotating orbits continue smoothly through this region. When the orbital frequency approaches the scale of the Bohr splitting, $\Omega \simeq |\epsilon_b|$, the overtone $|31-1\rangle$ gets excited, see Fig. 6.

Bohr resonance

Near $\Omega \simeq |\epsilon_b|$, the phase of the hyperfine mixing term in (3.29) oscillates rapidly over a time of order η^{-1}. In this region, we have $|c_d^{(h)}|^2 \sim (\eta/\Omega)^2 \sim (\eta/\epsilon_b)^2 \ll 1$, so that we can ignore the small correction due to the $|21-1\rangle$ state. The dynamical evolution, once again, reduces to a two-level

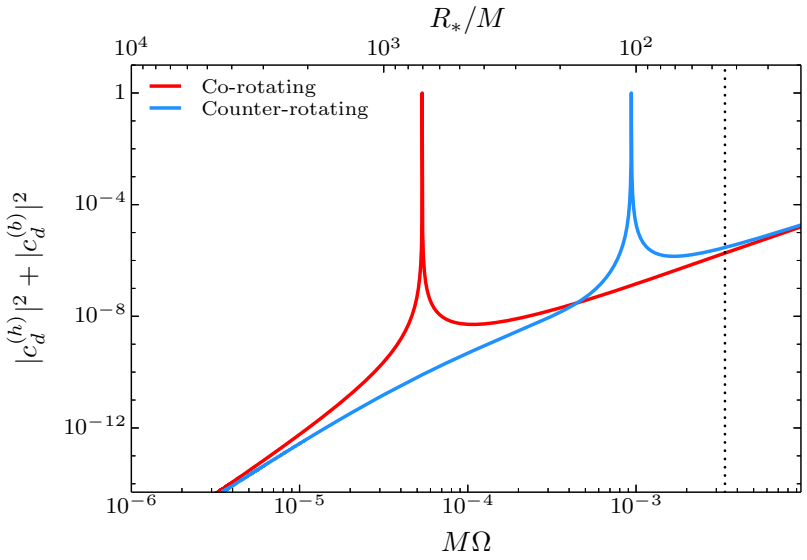

Figure 6: Evolution of the occupation density of the decaying modes, near the hyperfine and Bohr resonances, for co-rotating (red) and counter-rotating (blue) orbits, respectively. For illustration purposes, we use $\alpha = 0.3$ and $q = 10^{-3}$. The dotted vertical line denotes the characteristic Bohr radius of the $|211\rangle$ mode. For clarity, the oscillatory features of the solutions (3.25) and (3.31) have been omitted.

system, this time describing the mixing between the states $|211\rangle$ and $|31-1\rangle$. Repeating the analysis of §3.3.1, we find

$$|c_d^{(b)}(t)|^2 = \left[1 - \left(\frac{\epsilon_b \mp \Omega}{\Delta_R^{(b)}}\right)^2\right] \sin^2\left[\int_{t_0}^{t} \mathrm{d}t'\, \Delta_R^{(b)}(t')\right], \tag{3.31}$$

where the modified Rabi frequency is

$$\Delta_R^{(b)} \equiv \sqrt{(7.6\eta)^2 + (\epsilon_b \mp \Omega)^2}\,. \tag{3.32}$$

Similar to the hyperfine case, the system undergoes a resonance when the orbital frequency matches with the energy split with the overtones. We refer to this effect as the *Bohr resonance*. A crucial difference to the case discussed in §3.3.1 is that, while for the hyperfine resonance we have $\omega_{21-1} < \omega_{211}$, the Bohr resonance is for an excited state $\omega_{31-1} > \omega_{211}$; see Fig. 5. This implies that the Bohr resonance can only occur for counter-rotating orbits, at a binary separation given by

$$R_{\rm res}^{(b)} = \left(\frac{144}{5}\right)^{2/3} \alpha^{-2}(1+q)^{1/3}\, r_g\,. \tag{3.33}$$

Note the α^{-2} scaling, whereas the corresponding result for the hyperfine resonances scales as α^{-4}. For small α, the Bohr resonance therefore occurs at a much smaller separation than the hyperfine case (see Fig. 6). In terms of the Bohr radius of the cloud, we can write $R_{\rm res}^{(b)} =$

$(18/5)^{2/3}(1+q)^{1/3}\, r_c$. For $q < 1$, the Bohr resonance thus occurs at the boundary of the regime of validity of the multipole expansion, $R_* > r_c$. On the other hand, for $q \gg 1$, the multipole expansion remains accurate, while the stronger constraint typically comes from the requirement for the validity of the perturbative treatment of the gravitational interaction with negligible mass transfer, corresponding to $R_* > R_{\rm pt} = 2q^{1/3} r_c$.

3.4 Cloud Depletion

So far, we have taken the growing and decaying modes to be stationary, while in reality both have non-zero decay widths, see (2.12). Although Γ_{211} vanishes when the superradiant growth stops, the rates $\Gamma_{n\ell m}$, with $m \leq 0$, remain finite throughout the evolution of the BH-cloud. Since the gravitational perturbation of the companion can induce transitions to the decaying modes, this opens up a new depletion channel for the cloud. In this section, we will explore this effect in more detail, both for co-rotating and counter-rotating orbits.

As we shall see, it is convenient to express the time evolution of the system in terms of the orbital frequency, Ω, of the binary. For quasi-circular orbits, the relation between t and Ω due to the leading quadrupolar GW emission is [104]

$$t(\Omega) = \tau_0 \left[1 - \left(\frac{\Omega_0}{\Omega}\right)^{8/3}\right], \tag{3.34}$$

where τ_0 is the time to merger for an initial orbital frequency Ω_0:

$$\frac{\tau_0}{M_{\rm tot}} \equiv \frac{5}{256}\frac{1}{\nu}\left(\frac{1}{M_{\rm tot}\Omega_0}\right)^{8/3}, \tag{3.35}$$

with $M_{\rm tot} \equiv M + M_*$ and $\nu \equiv M M_*/M_{\rm tot}^2$. For simplicity, we will assume that we can neglect the GW emission from the cloud throughout the coalescence of the binary. For the case of real scalar fields, this requires the time to merger, τ_0, to be shorter than the lifetime of the cloud, τ_c, introduced in §2.3. For complex fields, this constraint does not apply. For the case of real fields, imposing the condition $\tau_0 < \tau_c$ leads to

$$\frac{\tau_0}{\tau_c} \simeq \frac{10^{-21}}{(M\Omega_0)^{8/3}}\,\frac{(1+q)^{1/3}}{q}\left(\frac{\alpha}{0.07}\right)^{15} < 1\,, \tag{3.36}$$

which can be translated into a bound on the initial orbital frequency

$$\Omega_0 \gtrsim 0.9\ {\rm mHz}\left(\frac{3M_\odot}{M}\right)\,\frac{(1+q)^{1/8}}{q^{3/8}}\left(\frac{\alpha}{0.07}\right)^{45/8} \equiv \Omega_{\rm cr}\,. \tag{3.37}$$

In the following, we will assume $\Omega > \Omega_{\rm cr}$ during the entirety of the binary inspiral. In principle, we can also study binaries which form at smaller initial orbital frequencies, so that GW emission depletes the cloud before merger. We will return to this point in §4.3.

Level mixings

We take t_0 to be the time at which the superradiance has saturated. To estimate the amount of depletion between times t_0 and t, we introduce the following quantity

$$\mathcal{A}(t, t_0) \equiv \sum_{n,\ell}\sum_{m\leq 0} |\Gamma_{n\ell m}| \int_{t_0}^{t} {\rm d}t' \left|c_{n\ell m}(t')\right|^2, \tag{3.38}$$

where $c_{n\ell m}(t)$ is the overlap of the state $|\psi\rangle$ with the decaying modes $|n\ell m\rangle$, with $m \leq 0$. The 'depletion estimator' (3.38) is thus the ratio of the integrated time spent by the system in the decaying modes to the decay timescale $|\Gamma_{n\ell m}|^{-1}$, weighted by the occupation density of each state. Physical quantities of the cloud, such as its mass and angular momentum, would decay as $e^{-2\mathcal{A}(t,t_0)}$, where the factor of 2 in the exponential arises because the energy-momentum tensor depends quadratically on the field. In the limit where mixing with the decaying states is negligible, $\mathcal{A} \to 0$ and the cloud remains stable. On the other hand, significant depletion occurs when $\mathcal{A}$ becomes of order one.

For $\alpha < 1$, the decay rate (2.12) is suppressed for higher ℓ's, so that the sum in (3.38) will be dominated by the modes with $\ell = 1$ and $m = -1$ (the $m = 0$ mode decouples for orbits along the equatorial plane). Restricting further to the dominant decaying channels, with $n_h = 2$ and $n_b = 3$,[11] and using (3.34) to convert the integral over time in (3.38) into an integral over orbital frequency, we have[12]

$$\mathcal{A}(\Omega, \Omega_0) \simeq \sum_{i=\{h,b\}} |\Gamma_d^{(i)}| \left[\frac{5}{96} \frac{1}{\nu} \frac{1}{M_{\rm tot}^{5/3}} \int_{\Omega_0}^{\Omega} \mathrm{d}\Omega' \, \Omega'^{-11/3} \left| c_d^{(i)}(\Omega') \right|^2 \right] . \tag{3.39}$$

Using Detweiler's approximation (2.12), the relevant decay rates are

$$|\Gamma_d^{(i)}| = \frac{B_{(i)}}{24} \frac{\alpha^{10}}{M} \left(\frac{1 - 4\alpha^2}{1 + 4\alpha^2} \right)^2 \left(\frac{2}{1 + 4\alpha^2} + \tilde{r}_+ \right) , \tag{3.40}$$

where $B_{(h)} \equiv 1$ and $B_{(b)} \equiv 256/729$, and we used $\tilde{a} = \tilde{a}_s$, at saturation. In the limit of small α, the corresponding decay time is

$$\begin{aligned} \tau_d^{(i)} &\simeq 1 \, B_{(i)}^{-1} \text{ years} \left(\frac{M}{3M_\odot} \right) \left(\frac{0.07}{\alpha} \right)^{10} , \\ &\simeq 0.9 \, B_{(i)}^{-1} \text{ years} \left(\frac{M}{10^5 M_\odot} \right) \left(\frac{0.2}{\alpha} \right)^{10} . \end{aligned} \tag{3.41}$$

This timescale is very sensitive to α, but can be shorter than the duration of GW observations, so that the decay can, in principle, occur in observational bands. In the following, we will use the estimator (3.39) to analyze the stability of the BH-cloud against level mixing, during the inspiral phase of the binary dynamics.

Co-rotating orbits

We first consider the evolution of the cloud for co-rotating orbits, which is dominated by the existence of the hyperfine resonance. For each combination of α and q, we chose the initial condition $\Omega_0 = \Omega_{\rm cr}$, see (3.37). Figure 7 illustrates the total amount of depletion due to level mixing between Ω_0 and the breakdown of perturbation theory at $\Omega_{\rm pt}$. As shown in the top panel of Fig. 7, the parameter space divides into three distinct regions:

[11] Ignoring the $n \geq 4$ overtones amounts to underestimating the total contribution from $n \geq 3$ by approximately a factor of 2, mostly from the evolution of the cloud prior to the resonances. This arises from the suppression of $\Gamma_{n\ell m}$ for increasing n, see (2.13).

[12] In the numerical integration of (3.39), we ignore the oscillatory terms in (3.25) and (3.31), which overestimates $\mathcal{A}$ by roughly a factor of 2.

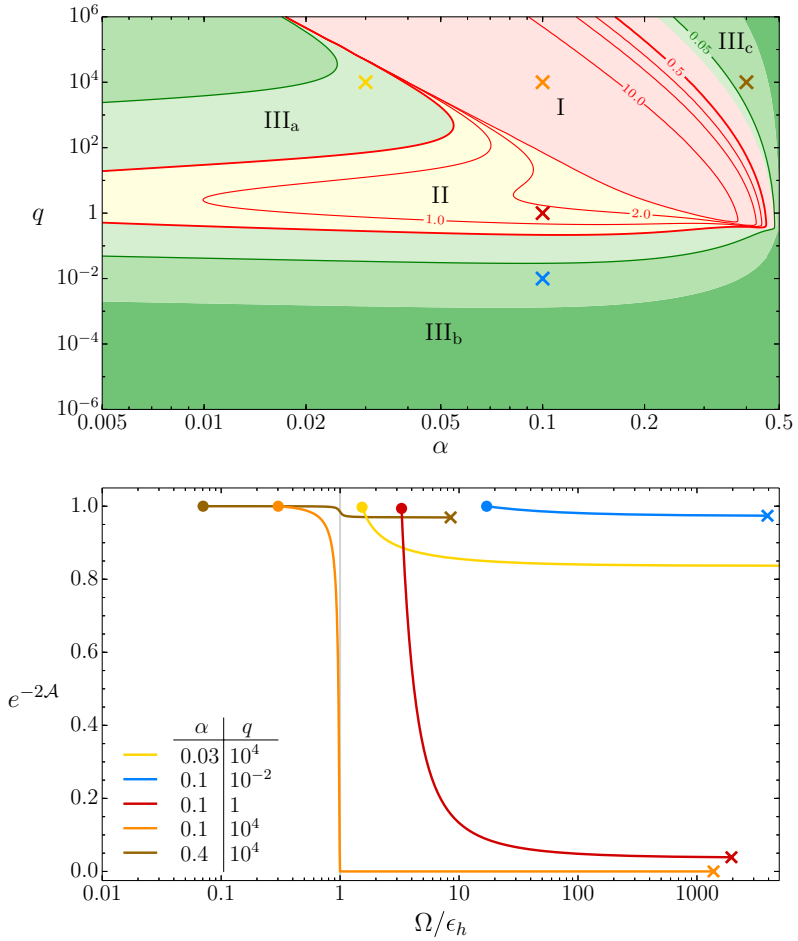

Figure 7: Plot of the total depletion of the cloud for co-rotating orbits. Shown is $\mathcal{A}(\Omega_{\rm pt}, \Omega_{\rm cr})$, as a function of q and α (*top*), and the evolution of $e^{-2\mathcal{A}}$ for specific choices of q and α (*bottom*). See the main text for further discussion.

- Region I (red). The cloud depletes dramatically during the resonance.
- Region II (yellow). The cloud experiences a long period of perturbative depletion.
- Region III (green). The cloud mostly survives the entire inspiral.

To understand the morphology of the parameter space, it is useful to compare the initial orbital frequency to that of the hyperfine resonance:

$$\frac{\Omega_0}{\epsilon_h} \simeq 2.9 \left(\frac{0.1}{\alpha}\right)^{11/8} \frac{(1+q)^{1/8}}{q^{3/8}} \,. \tag{3.42}$$

Only for $\Omega_0 < \epsilon_h$ is the hyperfine resonance experienced during the part of the evolution shown in Fig. 7. This occurs for $q \gtrsim 2 \times 10^{-4}\, \alpha^{-11/2}$, corresponding to regions I and III$_c$ of the parameter space. In the other regions, the initial orbit has already passed the orbital frequency of the hyperfine resonance.

As seen in the example $\{\alpha = 0.1, q = 10^4\}$ (*orange curve*), for combinations of parameters in region I, the cloud depletes dramatically during the hyperfine resonance. In region III$_c$, on

the other hand, the cloud survives the resonance, as illustrated for the case $\{\alpha = 0.4, q = 10^4\}$ (*brown curve*). This is because, for large q and α, the binary only spends a short amount of time within the resonance epoch, relative to the decay time $\tau_d^{(h)}$.[13]

The results in the other regions can be understood qualitatively as follows. The larger the value of q, for fixed M and α, the faster the binary transits through the inspiral stage, due to the efficiency of GW emission from the binary. At the same time, in the regime of perturbative level mixing, $|c_d|^2$ is proportional to q. Since $\mathcal{A}$ is roughly proportional to both the time spent in the inspiral and the strength of the coupling to the decaying modes, the two effects compete with each other. By continuity, $\mathcal{A}$ peaks at intermediate values of q in region II. As shown for the case $\{\alpha = 0.1, q = 1\}$ (*red curve*), the depletion can be significant, yet it extends over a larger time than in the case of the resonant decay. In regions III_a and III_b, the rapid decay of the orbit due to GW emission ($q \gg 1$) and the suppression of the perturbative mixing ($q \ll 1$) dominate, respectively. As a consequence, the cloud hardly depletes during the inspiral, as shown for $\{\alpha = 0.03, q = 10^4\}$ (*yellow curve*) and $\{\alpha = 0.1, q = 10^{-2}\}$ (*blue curve*). However, this does not necessarily imply that the cloud is stable beyond $\Omega > \Omega_{\rm pt}$, since our perturbative treatment of the problem starts breaking down. Only a full numerical simulation could then inform us about the fate of the cloud towards the merger stage.

Counter-rotating orbits

Next, we consider the case of counter-rotating orbits, for which the Bohr resonance can be excited. As before, we chose the initial condition $\Omega_0 = \Omega_{\rm cr}$. Figure 8 illustrates the total amount of depletion between Ω_0 and $\Omega_{\rm pt}$. The labelling of the different regions is in accordance to Fig. 7. Once again, the basic features can be understood as follows.

The ratio of the initial orbital frequency and the frequency of the Bohr resonance is given by:

$$\frac{\Omega_0}{\epsilon_b} \simeq 0.003 \left(\frac{\alpha}{0.1}\right)^{21/8} \frac{(1+q)^{1/8}}{q^{3/8}} \,. \tag{3.43}$$

Except for very large values of α and very small q, this implies $\Omega_0 < \epsilon_b$, so that essentially all the orbits shown in Fig. 8 experience the Bohr resonance at some point during the inspiral. However, since the Bohr resonance occurs at much smaller orbital separations than the hyperfine resonance, the binary moves through it much faster. As a consequence, the amount of depletion is significantly less dramatic than for co-rotating orbits experiencing the hyperfine decay. Nevertheless, for $\alpha \gtrsim 0.07$ and $q \lesssim 1$ (corresponding to region I in the figure), the Bohr resonance still creates a sharp depletion of the cloud, yet without termination. This is illustrated by the *blue curves* in the bottom panel of Fig. 8.

In region II, the cloud experiences a slow perturbative depletion—mostly controlled by mixing with the nearby hyperfine states—which can significantly reduce its energy density; see the *red curves* in Fig. 8. By the time the cloud reaches the Bohr resonance, the depletion (in comparison)

[13] For fixed mass of the BH-cloud, M, large values of q increase the rate of GW emission and hence the shrinking of the orbit, while larger values of α push the resonance towards shorter distances. Notice that, while the GW emission is invariant under $q \to 1/q$, the timescale associated with the decaying mode, as well as the separation at resonance, is controlled by M, which breaks this symmetry.

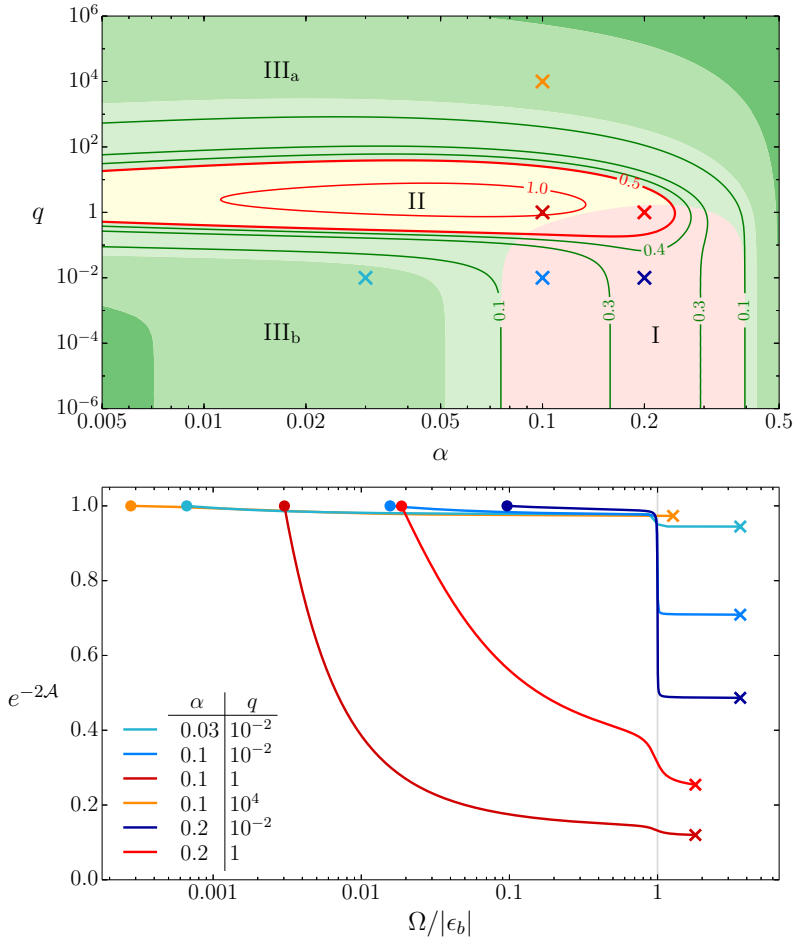

Figure 8: Same as Fig. 7, but for counter-rotating orbits. The resonance is less pronounced than for co-rotating orbits since the system moves through it much faster.

is only a small effect. In regions III$_a$ and III$_b$, the cloud survives with hardly any depletion, even after moving through the resonance.

4 Gravitational Wave Signatures

In this section, we will briefly sketch some of the observational consequences of our findings. For real scalar fields, there are two sources of GWs: *i*) the continuous emission from the rotating cloud itself (§4.1), and *ii*) the radiation produced by the binary (§4.2). For complex scalar fields, only the latter is present. These signals can be affected by the dynamics of the boson cloud as the system evolves during the inspiral. In §4.3, we will discuss a few paradigmatic examples of binary systems that can provide key information about the ultralight particles forming the cloud, and whose GW signatures are within reach of current and planned GW observatories. Our treatment will be rather schematic and a more detailed investigation will be the subject of future work.

4.1 Signal from the Cloud

As we have seen in §2.3, a real scalar cloud emits continuous, monochromatic GWs [69, 95]. The frequency of these GWs is determined by the mass of the scalar field,

$$f_c \simeq \frac{\mu}{\pi} = 484\,\mathrm{Hz}\,\left(\frac{\mu}{10^{-12}\ \mathrm{eV}}\right), \tag{4.1}$$

and their rms strain amplitude is [95, 99]

$$h_c \simeq 2\times 10^{-26}\left(\frac{M}{3M_\odot}\right)\left(\frac{M_c(\alpha)/M}{0.1}\right)\left(\frac{\alpha}{0.07}\right)^6\left(\frac{10\,\mathrm{kpc}}{d}\right), \tag{4.2}$$

where d is the (Euclidean) distance of the source. Since the signal is emitted continuously, its detectability depends on the total observation time $T_{\rm obs}$. The signal-to-noise ratio (SNR) of the cloud signal is

$$\mathrm{SNR} = h_c\,\langle F_+^2\rangle^{1/2}\frac{T_{\rm obs}^{1/2}}{\sqrt{S_n(f_c)}}, \tag{4.3}$$

where $S_n(f_c)$ is the (one-sided) noise spectral density at the frequency f_c, and $\langle F_+^2\rangle = \langle F_\times^2\rangle$ is the angular average of the square of the detector pattern functions $F_{+,\times}$ for each GW polarization. Using (4.2), we get

$$\mathrm{SNR} \simeq 13\,\langle F_+^2\rangle^{1/2}\left(\frac{T_{\rm obs}}{1\ \mathrm{yr}}\right)^{1/2}\left(\frac{10^{-23}\ \mathrm{Hz}^{-\frac{1}{2}}}{\sqrt{S_n(f_c)}}\right)\left(\frac{M}{3M_\odot}\right)\left(\frac{M_c/M}{0.1}\right)\left(\frac{\alpha}{0.07}\right)^6\left(\frac{10\,\mathrm{kpc}}{d}\right), \tag{4.4}$$

which is strongly dependent on α. We see that BH-cloud systems with $\alpha < 0.07$ and $M < 10^2\,M_\odot$ may be detectable only within our own galaxy, while those with larger values of α, and bigger masses, may be observed at extra-galactic distances. Further discussion and detailed forecasts can be found in [96, 105–107].

Resonant extinction/attenuation

When the BH-cloud is part of a binary system, the cloud may deplete over time, according to:[14]

$$\frac{h_c(t)}{h_c(t_0)} = \frac{M_c(t)}{M_c(t_0)} \sim e^{-2\mathcal{A}(t,t_0)}, \tag{4.5}$$

[14] The ratio (4.5) need not be a smooth exponential decay, but may contain periodic features; cf. (3.25) and (3.31). The depletion process switches on and off as the binary transits through the resonance. This effect manifests itself most prominently during the Bohr resonance.

where $\mathcal{A}$ is the depletion estimator introduced in (3.38). This decay is most prominent for co-rotating orbits, since the hyperfine resonance occurs at large separations, so that the binary spends a significant amount of time near the resonance orbit. For counter-rotating orbits, the Bohr resonance attenuates the signal, but does not completely terminate it. In either case, the extinction/attenuation of the GWs produced by the cloud turns into a unique feature of the binary system. In §4.3, we will discuss the phenomenological consequences of this effect in several case studies.

Doppler modulation

In the presence of a companion, the GW frequency f_c will also be modulated by the orbital motion.[15] In particular, if the orbital plane of the binary is oriented such that the BH-cloud has a non-vanishing radial velocity along the line-of-sight, the orbital motion will induce a periodic Doppler shift of the GW signal,

$$\frac{\Delta f_c}{f_c} = \frac{v_r}{c} = \left(\frac{M_*}{M_{\rm tot}}\right)\frac{R_*\Omega}{c}\sin\iota\,, \tag{4.6}$$

where v_r is the radial component of the velocity of the BH-cloud along the line-of-sight, and ι is its angle relative to the normal of the orbit. While detecting the periodic modulation of the frequency is experimentally (and computationally) challenging, this Doppler effect would be very convincing evidence that the BH-cloud is part of a binary system. At the same time, it will open a new avenue to infering parameters of a binary system at low orbital frequencies, by monitoring the signal from the cloud with continuous searches. Similar searches are being performed for neutron stars in binaries [109].

4.2 Signal from the Binary

The presence of the cloud can also reveal itself in the GW signal of the binary, through subtle modifications in the waveforms due to the cloud's multipole moments and the tidal response to the companion. In the following, we will show how these finite-size effects inherit a characteristic time dependence due to the dynamics of the cloud.

Spin-induced quadrupole

A spinning compact object has a series of multipole moments [110, 111] (see Appendix C). For the Kerr BH, the no-hair theorem [112, 113] implies that these moments are fixed completely by the mass and spin of the BH, while additional independent parameters are needed to characterize other objects, such as NSs [114, 115] or boson stars [116]. Given the mass quadrupole moment Q, it is customary to introduce the dimensionless parameter

$$\kappa \equiv -\frac{QM}{J^2}\,, \tag{4.7}$$

where M and J are the mass and angular momentum of the body. For Kerr BHs, we have $\kappa = 1$ [111], while for NSs, $\kappa \approx 1.4 - 8$, depending on the equation of state [114, 115]. The

[15] This is the same effect that famously led to the discovery of the Hulse-Taylor binary pulsar, where the frequency of the emitted electromagnetic radiation was found to be modulated by the orbital motion [108].

observation of a compact object with deviations from $\kappa = 1$, and masses larger than the estimated upper bound of NSs (around $3M_\odot$) [117], would be direct evidence for the existence of exotic objects in nature, see e.g. [29]. The value of κ can be obtained from the GW signal of the binary, through its effect on the phase of the signal [22, 27]. The effect arises at 2PN order, i.e. $\kappa v^4 \chi^2$, where v is the typical relative velocity of the binary and $\chi \equiv J/M^2$ is the dimensionless spin parameter.

As long as the mass of the boson cloud constitutes a sizable fraction of the initial BH mass, the metric of the (isolated) BH-cloud would depart from that of the Kerr background. These departures include spin-induced multipole moments, which are not uniquely determined by the mass and spin of the cloud. A rigorous computation of these quantities would require incorporating the backreaction on the spacetime geometry, which is beyond the scope of this work.[16] Instead, we will assume that the cloud dominates the contribution to the multipole moments of the BH-cloud, and estimate κ by comparing the cloud's mass quadrupole, Q_c, to J^2/M, where M and J are the *total* mass and angular momentum of BH-cloud system. We choose to normalize κ with (M, J) of the BH-cloud, instead of (M_c, J_c) of the cloud itself, because *i*) the quantities (M, J) can be directly measured through GW observations, and *ii*) they are conserved throughout the evolution (up to small losses due to GW emission). The parameters (M, J) therefore also coincide with the mass and angular momentum of the *initial* BH prior to the formation of the cloud.

From the stress-energy tensor of the scalar field, we find for the $|211\rangle$ state (see Appendix A)

$$\kappa(\alpha) \geq -\frac{Q_c(\alpha)}{M^3} \sim 10^3 \left(\frac{M_c(\alpha)/M}{0.1}\right)\left(\frac{0.1}{\alpha}\right)^4 , \tag{4.8}$$

where we have imposed the weak cosmic censorship condition, $J \leq M^2$ [119], to obtain the lower bound. The effect on the GW phase then scales as

$$\kappa(\alpha) v^4 \chi^2 \gtrsim 10^{-2} \left(\frac{M_c(\alpha)/M}{0.1}\right)\left(\frac{v}{\alpha/2}\right)^4 , \tag{4.9}$$

where we used $\chi \simeq 1$, and assumed that the initial BH is rapidly rotating (which is required for the cloud to form in the first place). Notice that, in the regime of validity of the perturbative expansion, the relative velocity satisfies $v \lesssim \alpha/2$.[17] For $v > \alpha/2$, the companion experiences a smaller amount of the cloud according to Gauss' law. Even though larger relative velocities may seem favorable, the reduction in the effective mass of the cloud will dominate, leading to negligible finite-size effects once the companion enters the BH-cloud system.

The existence of resonances in the orbital dynamics can lead to an abrupt drop, or significant change, in the mass of the cloud M_c, with a corresponding frequency-dependent variation of the GW signal. As the binary scans through the Rabi frequency, we have

$$\frac{\kappa(t) - 1}{\kappa(t_0) - 1} \sim \frac{M_c(t)}{M_c(t_0)} \sim e^{-2\mathcal{A}(t,t_0)} . \tag{4.10}$$

[16] Exact solutions with (complex) scalar hair around spinning BHs have been studied numerically in the literature, see e.g. [118]. In principle, these quasi-stationary spacetimes can also have $\kappa \gg 1$.

[17] For $q \lesssim 1$, the virial theorem implies $v \simeq (\alpha/2)\sqrt{r_c/R_*}$ and hence $v \lesssim \alpha/2$ in the regime of validity of the multipole expansion, $r_c < R_*$.

This time dependence constitutes a distinctive signature of the existence of a BH-cloud in a binary system and may leave a measurable imprint in the waveforms. We will return to this in §4.3.

Tidal deformations

In addition to the permanent multipole moments, a compact object may also acquire induced multipoles in the presence of a gravitational perturbation. It is an interesting (and somewhat puzzling) fact that for BHs the tidal response to an external field vanishes in four-dimensional Einstein gravity.[18] This is often parameterized in terms of the tidal Love numbers,[19] which are zero for black holes [7, 23, 24, 49, 50], but may have sizable values for neutron stars [23, 24] and other more exotic objects (like boson stars) [30, 31, 121]. While the Love numbers first enter in the GW phase at 5PN order [11, 25, 26, 122], the lack of standard model background in Einstein's theory offers a powerful opportunity to probe the dynamics of vacuum spacetimes in General Relativity, through precision GW data. See [7] for more on this issue.

Since the cloud is much less compact than an isolated BH, but carries a significant fraction of the mass and angular momentum of the system, we can, in principle, have large Love numbers for the BH-cloud system. Although a detailed computation is beyond the scope of this work, on dimensional grounds we expect the 'tidal deformability' parameter, Λ, to scale as (see Appendix C)

$$\Lambda(\alpha) \sim \left(\frac{M_c(\alpha)}{M}\right)\left(\frac{r_c}{2r_g}\right)^4 \sim 10^7 \left(\frac{M_c(\alpha)/M}{0.1}\right)\left(\frac{0.1}{\alpha}\right)^8 . \tag{4.11}$$

The parameter Λ enters in the phase of the waveform at 5PN order, and its imprint on the signal from the binary therefore scales as

$$\Lambda(\alpha)\, v^{10} \sim 10^{-6} \left(\frac{M_c(\alpha)/M}{0.1}\right)\left(\frac{\alpha}{0.1}\right)^2 \left(\frac{v}{\alpha/2}\right)^{10} , \tag{4.12}$$

where $v \lesssim \alpha/2$ in the regime of validity of the multipole expansion.

As for the spin-induced quadrupole, the presence of the binary companion can induce a characteristic time dependence of the Love numbers

$$\frac{\Lambda(t)}{\Lambda(t_0)} \sim \frac{M_c(t)}{M_c(t_0)} \sim e^{-2\mathcal{A}(t,t_0)} , \tag{4.13}$$

most notably for Bohr resonances, which occur at shorter binary separations.

As the companion progresses into the cloud and approaches the merger with the central BH, both the effects of the spin-induced quadrupole and Love numbers will be dominated by the Kerr solution. In particular, the contribution from the Love number will become negligible. By comparing the values obtained before and after the resonance, the variation of the spin-induced quadrupole and Love number(s) can turn into a key signature of the presence of a cloud in a binary system.

[18] So far, this has been shown to hold for non-rotating BHs. However, it is also expected to be the case for Kerr BHs. See e.g. [120] and references therein for progress along this direction.

[19] These Love numbers are the analog of susceptibilities in electrodynamics, which describe the response of a distribution of charge to an applied electric (or magnetic) field.

4.3 Probing Ultralight Scalars

In this section, we study the new ways in which ultralight scalars can be probed with binary inspirals. We will concentrate on paradigmatic GW sources for which both the hyperfine and Bohr resonances can play a major role, accessible to present and planned GW detectors.

To be able to probe the resonances, the lifetime of the cloud has to be sufficiently long, and the resonance sharp enough, to be detected within the operational time window of GW observatories:

1. *Cloud lifetime.* For real scalars, survival of the cloud until the resonance typically requires $\tau_c \gtrsim 10\,\text{Myr}$ for stellar-mass binaries, using generic lower bounds on the merger times [98]. For supermassive BHs, we conservatively take $\tau_c \gtrsim 1\,\text{Gyr}$ to account for the large uncertainties in the formation channels. Finally, the stability issue does not arise for complex fields.

2. *Resonant decay.* To observe significant resonant decay in the GW signal by present and future GW detectors, the typical decay time, τ_d, must be $\lesssim$ a few years.

Using (2.17) and (3.41) for τ_c and τ_d, respectively, these considerations typically select narrow ranges of α, depending on M. For stellar-mass BHs, we will be sensitive to $\alpha \simeq 0.07$ for real fields, while clouds of complex fields may be observed for larger values of α. On the other hand, for supermassive BHs with $M \gtrsim 10^5 M_\odot$, the constraint on the decay time $\tau_d \lesssim$ years implies $\alpha \gtrsim 0.2$, with larger values of α required for larger M. Even though this typically leads to $\tau_c \lesssim 1\,\text{Myr}$ for real fields, astrophysical processes such as accretion may alleviate the stability issue [99].[20]

In the following, we will discuss how boson clouds around BHs can be probed in continuous-wave and binary searches. In the former, the resonant decay of the monochromatic signal is surveyed with ground-based detectors and LISA, while in the latter, the focus is on the resonant depletion/attenuation of finite-size effects, observed through precision measurements in the GW emission from the two-body system with LISA.

Continuous-wave searches

The frequency of the signal from the cloud is shown in Fig. 9, for physically motivated values of α and M, cf. (4.1), and compared to the frequency bands of ground-based [123–127] and space-based [128–130] detectors, as well as pulsar timing arrays (PTAs) [131–136]. We see that ground-based experiments probe $M \lesssim 3 \times 10^3 M_\odot$, while LISA would give us access to $M \gtrsim 3 \times 10^3 M_\odot$. For LIGO, the majority of resolvable events with significant SNR are produced by galactic sources, cf. (4.4). The present binary event rates inferred from LIGO [137] indicate that the most promising sources in the galaxy are far from merging. Indeed, population synthesis codes [138–140] suggest that there are presently of the order of 10^5 to 10^6 galactic BH-BH and BH-NS binaries of comparable masses with orbital frequencies distributed in the mHz region. Provided a fraction of these binary systems transit through a resonant epoch, a sharp decay in the GW signal from the cloud may be observed. This is particularly suitable for the hyperfine decay, for which the orbital resonances for stellar-mass BH binaries fall naturally in the mHz region; see (4.14) below. However, due to the finite lifetime of the clouds, detecting this effect

[20] In general, we can relax the condition (3.36) for the cloud's stability by requiring the lifetime to be sufficiently long to reach the resonance after formation, e.g. $\tau_c \gtrsim 1\,\text{Myr}$, but not necessarily to last until merger.

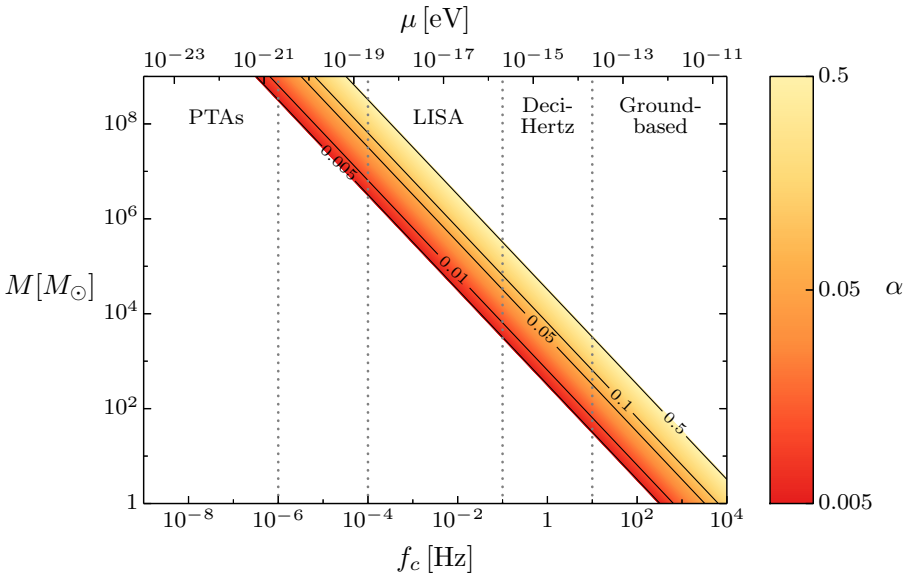

Figure 9: Frequency of the monochromatic signal for physically motivated ranges of α and M. The vertical dotted lines illustrate the typical observational bands of various GW observatories.

in the galaxy requires the clouds to be formed relatively recently, while the majority of these binaries may have formed much earlier [140]. Despite these inherent uncertainties in the binary formation mechanisms, there are fortunately a large number of galactic binaries, each sampling a distribution of initial conditions. This constitutes an *ensemble* which allows for a 'scanning' of the orbital frequencies for the resonance, and the corresponding depletion of the monochromatic GW signal.

The scanning for both the hyperfine and Bohr resonances is more promising with LISA, which would also be sensitive to extra-galactic sources. In particular, a sharp decay may be observed for clouds surrounding supermassive BHs with a small companion, in what are known as extreme-mass-ratio inspirals (EMRIs). Similarly to the tuning required for the binary signals from EMRIs to fall into the LISA band [141], a companion may excite orbital resonances, inducing a sharp depletion on the GW signal from a supermassive BH-cloud. The formation mechanism and population of intermediate-mass and supermassive BHs, as well as EMRIs, is less well-understood. However, since LISA will be able to probe sources of extra-galactic origin, the search volume increases considerably, allowing for the detection of GW signals at higher redshifts.

As a concrete example, consider a real scalar field with $\mu \simeq 10^{-17}$eV, forming a cloud surrounding a supermassive BH with mass $M \simeq 5 \times 10^6\, M_\odot$. For simplicity, let us assume that the BH accretes matter, so that the issue of the lifetime of the cloud may be ignored. In this scenario we have $\alpha \simeq 0.37$, and a resonant decay time of about a few months. The continuous monochromatic signal from the cloud occurs around $f_c \simeq 5\,$mHz, the most sensitive part of the LISA band. For binaries that transit through the hyperfine resonance, the complete termination of the signal occurs for $q \lesssim 10^2$. The decay can arise either from significant perturbative depletion in the early stages or, provided that the initial orbital frequency Ω_0 lies close to ϵ_h, the cloud may

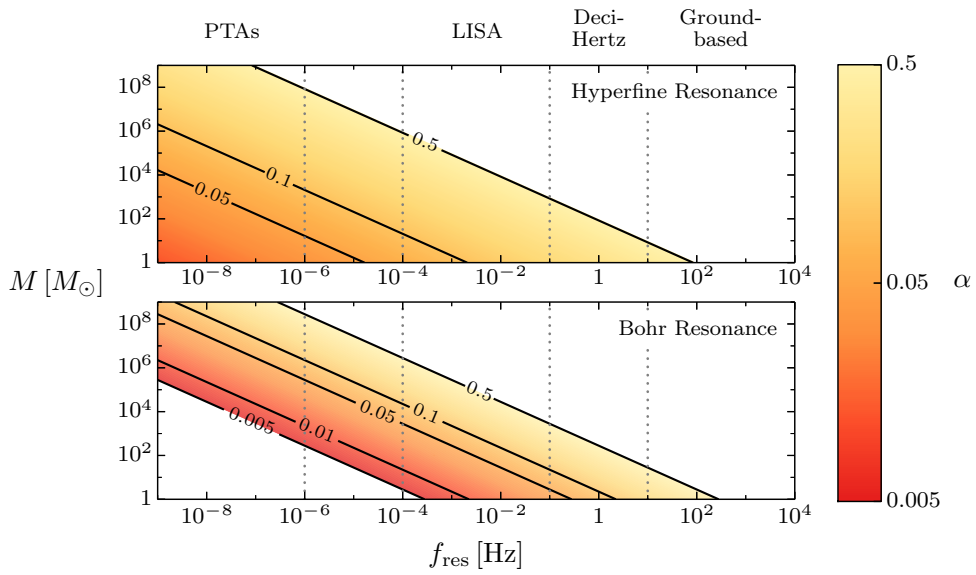

Figure 10: The resonance frequency $f_{\rm res}$ for physically motivated ranges of α and M. The vertical dotted lines illustrate the typical observational bands of various GW observatories.

survive the perturbative decay and experience a sharp depletion within a few months.[21] On the other hand, significant attenuation of the signal due to Bohr resonances requires $q < 1$, cf. Fig. 8. These type of binary systems, scanning over the space of orbital resonances, are expected to be abundant in nature, which motivates comprehensive continuous-wave searches with space-based interferometers.

Binary searches

Precision finite-size measurements in binary searches are a new probe of boson clouds around BHs. If the resonance falls within the frequency window of future observatories, it becomes a distinctive feature of the GW signal. To see when that may be the case, it is instructive to translate the orbital frequency at which the resonance transitions occur, $\Omega_{\rm res}$, to the GW frequency, $f_{\rm res}$, emitted from the binary during the inspiral:

$$f_{\rm res}^{(i)} \equiv \frac{\Omega_{\rm res}^{(i)}}{\pi} = \frac{|\epsilon_i|}{\pi} \simeq \begin{cases} 7.2\,{\rm mHz}\ \dfrac{1}{1+4\alpha^2}\left(\dfrac{\alpha}{0.1}\right)^7\left(\dfrac{3M_\odot}{M}\right), & \text{Hyperfine} \\ 0.75\,{\rm Hz}\ \left(\dfrac{\alpha}{0.1}\right)^3\left(\dfrac{3M_\odot}{M}\right). & \text{Bohr} \end{cases} \tag{4.14}$$

This frequency is shown in Fig. 10, for physically motivated ranges of α and M. We see that, for most cases, both the hyperfine and Bohr frequencies are too low to be observed by ground-based detectors. The best prospects for detecting the resonance feature in future binary searches is therefore through space-based detectors, such as LISA.

[21] One can show that for binary systems with initial condition $\Omega_0 < \epsilon_h$, Fig. 7 is modified such that regions II, III$_a$ and III$_b$ turn red, but not region III$_b$, making almost the entire parameter space susceptible to decay.

The targeted values of μ (and α) for real scalars is restricted mostly by the stability of the cloud. For complex fields, on the other hand, GW emission from the cloud is not present, and therefore binary searches are unconstrained, and perhaps the only way in which these bosons could be potentially observable.[22] As we see in Fig. 10, observing the resonant decay is most promising in the deci-Hertz and LISA frequency bands. For simplicity, let us focus on sources that are observable by LISA, which is sensitive to compact binaries with large masses $M \in [10^4, 10^7]\, M_\odot$, although in principle it can also detect stellar-mass BHs [142]. Binary searches can then broadly be divided into two classes: *i*) binaries of comparable masses, $q \in [10^{-2}, 10^2]$, and *ii*) EMRIs, with $q \in [10^{-6}, 10^{-2}] \cup [10^2, 10^6]$.

In the case of comparable-mass binaries, finite-size effects manifest themselves at high PN orders, and therefore become accessible when the relative velocity of the binary becomes sizable. Once the companion enters the cloud, the finite-size effects will be dominated by the BH solution, for instance the spin-induced quadrupole will be given by $\kappa \simeq 1$ and the Love numbers will vanish. To detect the time-dependent effects in (4.10) and (4.13), the imprints in the GW phase have to be observable near the resonance. For co-rotating orbits, where the hyperfine resonance occurs at larger distances, measuring the depletion of the finite-size effects is challenging. Nevertheless, it is also possible that the cloud forms in a binary systems with $\Omega_0 > \epsilon_h$, therefore missing the hyperfine resonance. While level mixings would still deplete the cloud, it is possible that it survives until later times; e.g. see Fig. 7 for $\alpha \simeq 0.1$ and $q \simeq 10^{-2}$. In this scenario, resonant depletion would not occur and finite-size effects may still be observed at later stages of the inspiral.

Detecting the resonant decay is more promising for counter-rotating orbits, where the resonance generically occurs at shorter separations. In that case, the relative velocity near the resonance is given by $v_{(b)} \simeq 0.65\,(\alpha/2)$, which can be significant. For example, for $\alpha \simeq 0.1$ and $M_c \simeq 0.1M$, the finite-size effects near the Bohr resonance are of order,

$$\kappa(\alpha)\, v_{(b)}^4\, \chi^2 \;\sim\; 10^{-3}\,, \tag{4.15}$$

$$\Lambda(\alpha)\, v_{(b)}^{10} \;\sim\; 10^{-8}\,. \tag{4.16}$$

The resonant depletion of these quantities can be as large as $\simeq 20 - 30\%$ (see Fig. 8 for $\alpha \simeq 0.1$ and $q \simeq 10^{-2}$). Notice that, while small, both types of finite-size effects are larger than the usual 2PN and 5PN terms, respectively. In particular, near the resonance, tidal effects are comparable to typical 3PN contributions and the corrections to the GW phase appear to be within reach of future GW observatories such as LISA [30].

In the case of EMRIs, the evolution of the companion in the background of a supermassive BH can be obtained through perturbative self-force computations [143, 144]. The tidal deformability of the object is typically not taken into account, since it is highly suppressed when $M_* \ll M$. Nonetheless, systems with $q \ll 1$ still offer an excellent probe of deviations from $\kappa = 1$ for the background spacetime. It has been estimated that a variation in the spin-induced quadrupole

[22] It is worth mentioning that in previous proposals, probes of scalar fields in binary systems rely on the formation of boson stars [31]. However, unlike the BH-cloud, boson stars do not experience resonant depletion, which therefore is a unique of feature of boson condensates surrounding spinning BHs.

of order $\Delta\kappa/\kappa \simeq 10^{-2}$ may be detectable by LISA [145]. For example, counter-rotating binaries with $\alpha \simeq 0.1 - 0.4$ and $q \lesssim 10^{-2}$ would behave in a similar way as the blue curves in Fig. 8. This strongly motivates searches for large spin-induced quadrupole moments in EMRIs and their resonant depletion.

5 Conclusions and Outlook

Astrophysical BHs exist with a wide range of masses, from a few to billions of solar masses. When these BHs are rapidly rotating, they can produce condensates of ultralight bosons with masses in the range $[10^{-20}, 10^{-10}]$ eV, which includes well-motivated candidates for physics beyond the Standard Model, such as the QCD axion [61–63], axion-like particles in string theory [66–68], and interesting new possibilities for dark matter [64]. Extremely ambitious observational programs are under way to search for these light particles in the lab [52], in astrophysics [83] and in cosmology [84–86]. As impressive as these efforts are, they are blind to particles that couple to ordinary matter only with gravitational strength. Such extremely weakly coupled particles would nevertheless be produced by BH superradiance. The resulting boson clouds can be long-lived (on cosmological/astrophysical timescales) creating temporary BH hair that can be searched for in future GW observations, either in isolation or as a member of a binary system.

In this paper, we studied the dynamics of scalar condensates in binary inspirals, both with real and complex fields. We showed that the presence of a companion greatly enriches the dynamics of the system, by inducing mixing between growing and decaying modes of the cloud. At certain critical orbital frequencies the evolution becomes non-perturbative, leading to enhanced mixing through resonances with the orbital motion of the system. By restricting to simplified two- and three-state models of the cloud, we have shown that the resulting time dependence can significantly affect physical observables through a sharp depletion (or at least an attenuation) of the energy density in the bosonic field. This has important phenomenological consequences, both for the monochromatic signal emitted by the cloud and the finite-size effects imprinted in the waveforms of the binary signal. The characteristic time dependence of the signals thus become a very distinctive feature of the dynamics of boson clouds in binary systems, which would not be present in other scenarios, e.g. boson stars.

The results presented here should be considered a first step towards more accurate descriptions of the dynamics of the cloud. For instance, a proper calculation of the finite-size effects associated with the BH-cloud will require numerical simulations, to incorporate the backreaction on the background geometry. We have also ignored the backreaction on the BH mass and spin due to the evolution of the surrounding cloud. In principle, an increase in the spin of the BH during the cloud's depletion could trigger its repopulation through superradiance, leading to a feedback mechanism that may be also imprinted in the GW signals. Moreover, our analytical treatment breaks down when higher modes are excited during the resonances, as well as during the late stages of the inspiral, where the dynamical system becomes strongly time dependent. In these cases, only numerical approaches are able to properly inform us about the exact details of the dynamics. Other aspects of our estimations can also be improved upon. For example, we have restricted our analysis to quasi-circular orbits on the equator. This was only for simplicity, and

it would be relatively straightforward to extend our analysis to the case of elliptic orbits. Finally, we did not perform a detailed forecast of the expected event rates, and signal strengths, with future GW observatories. This requires a careful treatment of formation mechanisms, as well as the associated generation of boson clouds.

In spite of our simplifications, we have identified robust GW signatures for clouds in binary inspirals, which open up new ways of probing physics beyond the Standard Model through current and future GW observations. In particular, we hope that future measurements could not only detect these ultralight particles, but also help us elucidate their putative properties. Following an analogy with collider physics, we expect to extract not only the particle's masses, but also their spins and self-couplings [146], ultimately realizing the idea of the 'gravitational collider'.

Acknowledgements

We thank Mina Arvanitaki, Masha Baryakhtar, Alessandra Buonanno, William East, Lotte ter Haar, Tanja Hinderer, Luis Lehner, Ilya Mandel, Mehrdad Mirbabayi, David Nichols, Samaya Nissanke, Paolo Pani, Frans Pretorius, John Stout, Ka Wa Tsang, Benjamin Wallisch, and Matias Zaldarriaga for helpful discussions. We thank Benjamin Wallisch for assistance in producing some of the figures. D. B. is grateful to the Leung Center for Cosmology and Particle Astrophysics at the National Taiwan University and the Institute for Advanced Study for hospitality while some of this work was being performed. The work of D. B. is supported by a Vidi grant of the Netherlands Organisation for Scientific Research (NWO) that is funded by the Dutch Ministry of Education, Culture and Science (OCW). The work of H. S. C. is supported by NWO. The work of R.A.P. was supported by the Simons Foundation and São Paulo Research Foundation Young Investigator Awards, grants 2014/25212-3 and 2014/10748-5, and by the German Science Foundation (DFG) within the Collaborative Research Center (SFB) 676 'Particles, Strings and the Early Universe.' R.A.P. would like to thank the International Center for Theoretical Physics (ICTP) in Trieste for hospitality while this work was being completed. R.A.P. is grateful to Leonidas K. Porto, Emiliano A. Porto and Imme Roewer for the unconditional support.

A Gravitational Atom

In this appendix, we derive some of the properties of the BH-cloud presented in the main text. In particular, we compute the corrections to the frequency eigenvalues of the Hamiltonian in the non-relativistic limit. We also determine the mass quadrupole moment of the BH-cloud in the Newtonian approximation. Unless stated otherwise, these results apply to both real and complex scalar fields.

Kerr geometry

The Kerr metric in Boyer-Lindquist (BL) coordinates is

$$\mathrm{d}s^2 = -\frac{\Delta}{\rho^2}\left(\mathrm{d}t - a\sin^2\theta\,\mathrm{d}\phi\right)^2 + \frac{\rho^2}{\Delta}\mathrm{d}r^2 + \rho^2\,\mathrm{d}\theta^2 + \frac{\sin^2\theta}{\rho^2}\left(a\mathrm{d}t - (r^2+a^2)\,\mathrm{d}\phi\right)^2 , \tag{A.1}$$

where we have defined

$$\Delta \equiv r^2 - 2Mr + a^2 \quad \text{and} \quad \rho^2 \equiv r^2 + a^2\cos^2\theta\,. \tag{A.2}$$

Since the metric components have no explicit dependence on t and ϕ, the Kerr spacetime is stationary and axisymmetric. The roots of Δ determine the event horizon at $r_+ = M+\sqrt{M^2-a^2}$ and the Cauchy horizon at $r_- = M-\sqrt{M^2-a^2}$. The surface $g_{tt}=0$ at $r_{\rm E} = M+\sqrt{M^2-a^2\cos^2\theta}$ is the ergosphere. The angular velocity of the spinning BH at its event horizon is

$$\Omega_{\rm H} = \frac{a}{2Mr_+}\,. \tag{A.3}$$

The BH angular velocity $\Omega_{\rm H}$ plays a crucial role in the superradiance condition (2.1).

Test scalar field

The Lagrangian of a free scalar field is

$$\mathcal{L} = \begin{cases} -\dfrac{1}{2}g^{ab}\nabla_a\Psi\nabla_b\Psi - \dfrac{1}{2}\mu^2\Psi^2 & \Psi \text{ real}\,, \\ -g^{ab}\nabla_a\Psi^*\nabla_b\Psi - \mu^2\Psi^*\Psi & \Psi \text{ complex}\,. \end{cases} \tag{A.4}$$

Ignoring the backreaction of the field's stress-energy on the metric, we can use the Kerr solution (A.1) for the metric g^{ab}. Expressed in BL coordinates, the Klein-Gordon equation is separable into a set of ordinary differential equations. To find the stationary solutions of the KG equation, we consider the following ansatz

$$\Psi(t,r,\theta,\phi) = \begin{cases} \displaystyle\sum_{\ell m}\int\frac{\mathrm{d}\omega}{2\pi}\ \mathrm{Re}\left[e^{-i\omega t}e^{im\phi}R_{\ell m}(r)S_{\ell m}(\theta,c)\right] & \Psi \text{ real}\,, \\ \displaystyle\sum_{\ell m}\int\frac{\mathrm{d}\omega}{2\pi}\ e^{-i\omega t}e^{im\phi}R_{\ell m}(r)S_{\ell m}(\theta,c) & \Psi \text{ complex}\,. \end{cases} \tag{A.5}$$

The plane wave solutions in t and ϕ are a direct consequence of the isometries of the Kerr solution. The angular functions $S_{\ell m}(\theta,c)$ are called spheroidal harmonics with spheroidicity parameter $c^2 \equiv a^2(\omega^2-\mu^2)$. In the limit $c^2\to 0$, we have $S_{\ell m}(\theta)e^{im\phi} \to Y_{\ell m}(\theta,\phi)$, where $Y_{\ell m}$ are the ordinary spherical harmonics. The radial functions $R_{\ell m}(r)$ do not admit analytic solutions and have to be determined numerically. However, as we shall see, at leading order in an expansion in r^{-1}, they take the form of the radial functions of the hydrogen atom.

Non-relativistic limit

The ansatz (A.5) corresponds to stationary solutions of a massive scalar field around the BH. To study the *dynamical* evolution of Ψ, it proves useful to make another ansatz

$$\Psi(t,\mathbf{r}) = \begin{cases} \dfrac{1}{\sqrt{2\mu}}\left[\psi(t,\mathbf{r})\, e^{-i\mu t} + \psi^*(t,\mathbf{r})\, e^{+i\mu t}\right] & \Psi \text{ real}\,, \\ \dfrac{1}{\sqrt{2\mu}}\,\psi(t,\mathbf{r})\, e^{-i\mu t} & \Psi \text{ complex}\,, \end{cases} \tag{A.6}$$

where ψ is a *complex* scalar field which varies on a timescale that is much longer than μ^{-1}. The action for ψ reads

$$S = \int \mathrm{d}^4x\sqrt{-g}\left(-\frac{1}{2\mu}\left[\nabla_a\psi^*\nabla^a\psi + i\mu g^{0a}\left(\psi^*\nabla_a\psi - \psi\nabla_a\psi^*\right) + \mu^2(g^{00}+1)\psi^*\psi\right]\right), \tag{A.7}$$

which spontaneously breaks time reparametrization. Expanding in powers of r^{-1}, we obtain the following effective action

$$S = \int \mathrm{d}t\mathrm{d}r\mathrm{d}\theta\mathrm{d}\phi\, r^2\sin\theta\left[\mathcal{L}_2 + \mathcal{L}_4 + \mathcal{L}_5 + \cdots\right], \tag{A.8}$$

where $\mathcal{L}_n$ denotes terms of order $\mathcal{O}(\alpha^n)$,

$$\begin{aligned} \mathcal{L}_2 &\equiv i\psi^*\partial_t\psi - \frac{1}{2\mu}\partial_r\psi^*\partial_r\psi - \frac{1}{2\mu r^2}\partial_\theta\psi^*\partial_\theta\psi - \frac{1}{2\mu r^2\sin^2\theta}\partial_\phi\psi^*\partial_\phi\psi + \frac{\alpha}{r}\psi^*\psi\,, \\ \mathcal{L}_4 &\equiv \frac{1}{2\mu}\partial_t\psi^*\partial_t\psi + \frac{2M}{r}\left[i\psi^*\partial_t\psi + \frac{1}{2\mu}\partial_r\psi^*\partial_r\psi + \frac{\alpha}{r}\psi^*\psi\right], \\ \mathcal{L}_5 &\equiv \frac{2iaM\psi^*\partial_\phi\psi}{r^3}\,. \end{aligned} \tag{A.9}$$

For the power counting, we have used the fact that $\alpha < 1$ and $r \sim r_c \simeq (\mu\alpha)^{-1}$. The Lagrangian $\mathcal{L}_2$ defines the non-relativistic limit, which leads to the Schrödinger equation

$$i\frac{\partial}{\partial t}\psi(t,\mathbf{r}) = \left[-\frac{1}{2\mu}\nabla^2 - \frac{\alpha}{r}\right]\psi(t,\mathbf{r})\,. \tag{A.10}$$

This is analogous to the non-relativistic limit of the hydrogen atom. By expanding ψ in terms of the stationary eigenstates

$$\psi(t,\mathbf{r}) = \int\frac{\mathrm{d}\omega}{2\pi}\sum_{\ell m}\psi_{n\ell m}(t,\mathbf{r})\,, \tag{A.11}$$

and using (A.5), we can identify

$$\psi_{n\ell m}(t,r,\theta,\phi) \simeq e^{-i(\omega-\mu)t}\bar{R}_{n\ell}(r)Y_{\ell m}(\theta,\phi)\,, \tag{A.12}$$

where we have used the small spheroidicity approximation $S_{\ell m}(\theta)e^{im\phi} \simeq Y_{\ell m}(\theta,\phi) + \mathcal{O}(\alpha^2)$, and defined $\bar{R}_{n\ell}(r) \equiv \sqrt{\mu/2}R_{\ell m}(r)$ for real Ψ, and $\bar{R}_{n\ell}(r) \equiv \sqrt{2\mu}R_{\ell m}(r)$ for complex Ψ. Since we have expanded the action in (A.8) at large distances, the boundary condition at the BH event

horizon is replaced by a regular boundary condition at the origin. The radial function $\bar{R}_{n\ell}(r)$ therefore take the form of the radial functions of the hydrogen atom.

The Lagrangians $\mathcal{L}_4$ and $\mathcal{L}_5$ are higher-order self-interaction terms. Using the non-relativistic equation of motion (A.10), we can substitute $i\partial_t\psi$ and $\partial_\phi\psi = im\psi$ back into $\mathcal{L}_4$ and $\mathcal{L}_5$. This gives

$$\mathcal{L}_4 + \mathcal{L}_5 = \frac{1}{2\mu}\partial_t\psi^*\partial_t\psi + \frac{\alpha}{\mu^2 r^3}\psi^*\left[\ell(\ell+1) - 2r\partial_r(r\partial_r) - 2\tilde{a}m\alpha\right]\psi\,, \tag{A.13}$$

where we have used the eigenvalue equation of the spherical hamornics

$$\left(\frac{1}{\sin\theta}\frac{\partial}{\partial\theta}\sin\theta\frac{\partial}{\partial\theta} + \frac{1}{\sin^2\theta}\frac{\partial^2}{\partial^2\phi}\right)Y_{\ell m}(\theta,\phi) = -\ell(\ell+1)Y_{\ell m}(\theta,\phi)\,. \tag{A.14}$$

Finally, it is convenient to write the dynamics of ψ in terms of the Hamiltonian

$$H_c \equiv T_c + V_c\,, \tag{A.15}$$

where we have separated H_c into its kinetic and potential components,

$$\begin{aligned} T_c &\equiv -\frac{1}{2\mu}\nabla^2 + \frac{1}{2\mu}\partial_t^2\,, \\ V_c &\equiv -\frac{\alpha}{r} - \frac{\alpha}{\mu^2 r^3}\left[\ell(\ell+1) - 2r\partial_r(r\partial_r)\right] + \frac{2\tilde{a}m\alpha^2}{\mu^2 r^3}\,. \end{aligned} \tag{A.16}$$

We see that the eigenfunctions of the cloud are determined by the Hamiltonian of a test particle of mass μ. Furthermore, since the Kerr metric is stationary, the kinetic energy of the BH vanishes. However, as we will see in Appendix B, this contribution becomes important when the BH-cloud is part of a binary system.

Frequency eigenvalues

Including the mass term μ that was factored out in (A.6), the eigenfrequency spectrum of the Hamiltonian (A.15) is

$$\omega_{n\ell m} = \mu\left(1 - \frac{\alpha^2}{2n^2} - \frac{\alpha^4}{8n^4} + \frac{(2\ell - 3n + 1)\,\alpha^4}{n^4(\ell+1/2)} + \frac{2\tilde{a}m\alpha^5}{n^3\ell(\ell+1/2)(\ell+1)}\right), \tag{A.17}$$

where we have used the following identities

$$\begin{aligned} \left\langle r^{-1}\right\rangle_{n\ell} &= \frac{\mu\alpha}{n^2}\,, \\ \left\langle r^{-2}\right\rangle_{n\ell} &= \frac{\mu^2\alpha^2}{n^3(\ell+1/2)}\,, \\ \left\langle r^{-3}\right\rangle_{n\ell} &= \frac{\mu^3\alpha^3}{n^3\ell(\ell+1/2)(\ell+1)}\,, \quad \ell > 0 \\ \left\langle r^{-2}\partial_r\left(r\partial_r\right)\right\rangle_{n\ell} &= \frac{\mu^3\alpha^3}{n^4}\left(\frac{\ell - n + 1/2}{\ell+1/2}\right), \end{aligned} \tag{A.18}$$

with $\langle\cdots\rangle_{n\ell}$ defined as the expectation value with respect to $\bar{R}_{n\ell}(r)$. Equation (A.17) shows that the frequency eigenvalues of modes with different quantum numbers $\{n\ell m\}$ are different. It is precisely these differences in the eigenfrequencies that allow level mixings to occur.

Klein-Gordon norm

The action (A.7) is invariant under the global $U(1)$ transformation $\psi \to \psi\, e^{-i\beta}$, where β is an arbitrary constant. The associated Noether current is

$$J^a = \frac{i}{2\mu}\left[\psi\nabla^a\psi^* - \psi^*\nabla^a\psi\right] - g^{0a}\psi^*\psi\,. \tag{A.19}$$

At leading order in the expansion in r^{-1}, the conserved charge is $J^0 \simeq \psi^*\psi$, which can be interpreted as the occupation density of a particular state. This is analogous to the probability density in quantum mechanics, after suitable normalization.

Quadrupole moment

The conserved energy associated with the energy-momentum tensor of the scalar field is

$$E \equiv -\int_\Sigma T^0{}_a k^a\,, \tag{A.20}$$

where $k^a = \delta^a{}_0$ is the time-like Killing vector field of the Kerr metric and Σ is a spacelike hypersurface of constant t. At leading order in r^{-1} and α, the energy density of the $|211\rangle$ mode of the cloud is

$$\rho_E(t,\mathbf{r}) \equiv -T^0{}_0 \simeq \frac{A^2\mu^6\alpha^5}{64\pi}\, r^2 e^{-\alpha\mu r}\sin^2\theta\,, \tag{A.21}$$

where A is the amplitude of the scalar field, which is determined by the efficiency of the superradiant instability. At leading order in α, the energy density ρ_E is equal to the mass density ρ_m of the cloud and the mass quadrupole moment can be approximated by

$$Q_c = \int_0^\infty \mathrm{d}r \int_0^\pi \mathrm{d}\theta \int_0^{2\pi} \mathrm{d}\phi\; r^2\sin\theta\,\left[\rho_m r^2 P_2(\cos\theta)\right], \tag{A.22}$$

where $P_2(\cos\theta)$ is the Legendre polynomial. Normalizing the amplitude A in (A.22) by the mass of the cloud

$$M_c = \int_0^\infty \mathrm{d}r \int_0^\pi \mathrm{d}\theta \int_0^{2\pi} \mathrm{d}\phi\; r^2\sin\theta\,\rho_m\,, \tag{A.23}$$

we obtain

$$Q_c \simeq -\frac{6M_c}{\alpha^2\mu^2} \simeq -\frac{3}{8}M_c r_c^2\,. \tag{A.24}$$

The negative sign arises as a direct consequence of the spinning motion of the cloud.

B Free-Falling Clouds

In §3.1, we derived the effect of the companion on the BH-cloud by considering the perturbed metric in Fermi coordinates. In this appendix, we present an alternative perspective of this derivation by considering a *three-body analogy*. Our main goal is to show how a fictitous dipole in the gravitational potential, generated by a change of coordinates, cancels out.

Three-body analogy

The eigenfunctions of the cloud are determined by the Hamiltonian H_c of a test particle of mass μ, cf. (A.15). This is analogous to the Hamiltonian of the electron in a hydrogen atom: while the electron wavefunction, as a solution of the Schrödinger equation, has a wave-like distribution around its nucleus, it is treated as a point particle at the level of the Hamiltonian. In the rest of this appendix, we will adopt this particle picture of the Hamiltonian.

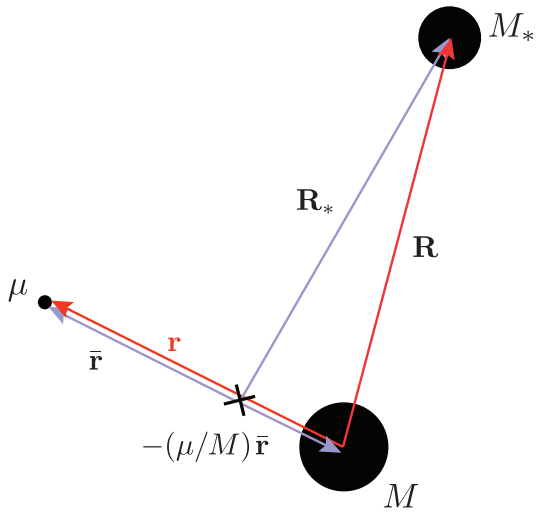

Figure 11: Coordinates of the effective three-body system.

In the presence of a companion, of mass M_*, the BH-cloud will accelerate due to the external gravitational field. The Hamiltonian (A.15) must hence be modified to include both the kinetic term of M as well as the contributions from M_*. It is convenient to introduce the center-of-mass coordinate, $\boldsymbol{\rho} \equiv (M\mathbf{r}_1 + \mu\mathbf{r}_2)/(M+\mu)$, so that the total Hamiltonian $H_{\rm tot}$ of the three-body system can be written as

$$H_{\rm tot} = \left[\frac{\mathbf{p}_\rho^2}{2(M+\mu)} + \frac{\mathbf{p}_r^2}{2\hat{\mu}} + V_c(|\mathbf{r}|)\right] + \left[\frac{\mathbf{p}_*^2}{2M_*} + V_*(\bar{\mathbf{r}}, \mathbf{R}_*)\right], \tag{B.1}$$

where $\mathbf{r} \equiv \mathbf{r}_2 - \mathbf{r}_1$ is the relative spatial separation between μ and M, and we introduced the reduced mass $\hat{\mu} \equiv M\mu/(M+\mu)$, the momenta $\mathbf{p}_\rho \equiv (M+\mu)\dot{\boldsymbol{\rho}}$ and $\mathbf{p}_r \equiv \hat{\mu}\dot{\mathbf{r}}$, and the coordinates $\mathbf{R}_* \equiv \{R_*, \Theta_*, \Phi_*\}$ and $\bar{\mathbf{r}} \equiv \{\bar{r}, \bar{\theta}, \bar{\phi}\}$ relative to the center-of-mass (cf. Fig. 11). Working in the

Newtonian limit, the external potential V_* is given by

$$\begin{aligned} V_*(\bar{\mathbf{r}}, \mathbf{R}_*) &= -\frac{M_* M}{|\mathbf{R}_* + \mu\bar{\mathbf{r}}/M|} - \frac{M_*\mu}{|\mathbf{R}_* - \bar{\mathbf{r}}|} \\ &= -M_* \sum_{\ell_* m_*} \frac{4\pi}{2\ell_*+1} \left(\frac{M(-\mu/M)^{\ell_*} + \mu}{R_*}\right) \left(\frac{\bar{r}}{R_*}\right)^{\ell_*} Y^*_{\ell_* m_*}(\Theta_*, \Phi_*)\, Y_{\ell_* m_*}(\bar{\theta}, \bar{\phi})\,. \end{aligned} \tag{B.2}$$

Substituting $\bar{\mathbf{r}} = (1+\mu/M)^{-1}\,\mathbf{r}$, and expanding in $\mu/M \ll 1$, we find

$$\begin{aligned} V_*(r, R_*) &= -\frac{M_*(M+\mu)}{R_*} - \frac{M_*\mu}{R_*} \sum_{\ell_*\geq 2} \sum_{|m_*|\leq \ell_*} \frac{4\pi}{2\ell_*+1} \left(\frac{r}{R_*}\right)^{\ell_*} Y^*_{\ell_* m_*}(\Theta_*, \Phi_*)\, Y_{\ell_* m_*}(\theta, \phi)\,, \\ &\equiv V_{*,0}(R_*) + \sum_{\ell_*\geq 2} V_{*,\ell_*}(r, R_*)\,. \end{aligned} \tag{B.3}$$

The leading monopole term $V_{*,0}$ determines the acceleration of the center-of-mass of the BH-cloud system. It doesn't depend on the relative separation $\mathbf{r}$, so it doesn't lead to a shift in the energy levels or the mode functions of the system. The remaining terms are a sum over harmonics, starting with the quadrupole $\ell_* = 2$. Importantly, the dipole contribution $\ell_* = 1$ vanishes in the center-of-mass frame.

Fictitious dipole

We have shown that the contribution from the dipole vanishes in the centre-of-mass frame. By virtue of the equivalence principle, this property must hold for all coordinate systems. More generally, this is a manifestation of the fact that a constant gravitational gradient — in this case the dipole term induced by the external gravitational field produced by the companion M_* — is physically unobservable. We now show explicitly that this is indeed the case for the coordinate system centered at M.

Consider expressing $H_{\rm tot}$ in terms of $(\mathbf{r}_1, \mathbf{r})$ instead of $(\boldsymbol{\rho}, \mathbf{r})$,

$$H_{\rm tot} = \left[\left(1+\frac{\mu}{M}\right)\left(\frac{\mathbf{p}_1^2}{2M} + \frac{\mathbf{p}_r^2}{2\hat{\mu}}\right) + \frac{\mu}{M\hat{\mu}}\mathbf{p}_1\cdot\mathbf{p}_r + V_c(|\mathbf{r}|)\right] + \left[\frac{\mathbf{p}_*^2}{2M_*} + V_*(\mathbf{r}, \mathbf{R})\right], \tag{B.4}$$

where the gravitational potential in this choice of coordinates reads (cf. Fig.11)

$$V_*(\mathbf{r}, \mathbf{R}) = -\frac{M_* M}{|\mathbf{R}|} - \frac{M_*\mu}{|\mathbf{R}-\mathbf{r}|}\,. \tag{B.5}$$

Expanding V_* for $r \ll R$ produces a dipole term

$$-\frac{M_*\mu}{|\mathbf{R}-\mathbf{r}|} \supset -\left(\frac{M_*\mu}{R}\right)\left(\frac{\hat{\mathbf{n}}\cdot\mathbf{r}}{R}\right), \tag{B.6}$$

where $\hat{\mathbf{n}}$ is the unit vector along $\mathbf{R}$, and we have used $|\mathbf{R}-\mathbf{r}| = R - \hat{\mathbf{n}}\cdot\mathbf{r} + \mathcal{O}(r^2)$. We will now show that this dipole is cancelled by the kinetic mixing term $\mu\,\mathbf{p}_1\cdot\mathbf{p}_r/M\hat{\mu}$. This is manifested most transparently in the $M_*/R \gg V_*$ limit, in which the gravitational attraction between M and

μ is negligible, compared to the force exerted by M_*. In this limit, M and μ free fall separately under the gravitational influence of M_*:

$$\dot{\mathbf{r}}_1^2 = \frac{2M_*}{R}\,, \qquad \dot{\mathbf{r}}_2^2 = \frac{2M_*}{|\mathbf{R}-\mathbf{r}|}\,, \tag{B.7}$$

and the angle between $\dot{\mathbf{r}}_1$ and $\dot{\mathbf{r}}_2$, denoted by γ, is given by

$$\cos\gamma = \frac{R^2 + |\mathbf{R}-\mathbf{r}|^2 - r^2}{2R|\mathbf{R}-\mathbf{r}|}\,. \tag{B.8}$$

The dipole arising from the kinetic mixing becomes,

$$\begin{aligned}
\frac{\mu}{M\hat{\mu}}\mathbf{p}_1\cdot\mathbf{p}_r &= \mu(\dot{\mathbf{r}}_1\cdot\dot{\mathbf{r}}_2 - \dot{\mathbf{r}}_1^2) \\
&= \mu\left(\frac{M_*(R^2+|\mathbf{R}-\mathbf{r}|^2-r^2)}{(R|\mathbf{R}-\mathbf{r}|)^{3/2}} - \frac{2M_*}{R}\right) \\
&= \mu\left[\frac{M_*}{R}\left(2+\frac{\hat{\mathbf{n}}\cdot\mathbf{r}}{R}\right) - \frac{2M_*}{R} + \mathcal{O}\left(\frac{r}{R}\right)^2\right] \\
&= +\left(\frac{M_*\mu}{R}\right)\left(\frac{\hat{\mathbf{n}}\cdot\mathbf{r}}{R}\right) + \mathcal{O}\left(\frac{r}{R}\right)^2\,.
\end{aligned} \tag{B.9}$$

As advertised, this precisely cancels the dipole contribution in (B.6).

C EFT of Extended Objects

In the language of effective field theory, spinning extended objects are described in terms of an effective worldline action [11–22, 28, 33–38]. One of the virtues of the formalism is the inclusion of finite-size effects as a series of higher-dimension terms beyond the 'minimally coupled' point-particle worldline action, $S_{\rm pp} = M\int \mathrm{d}\tau$, where M and τ are the mass and proper time, respectively. One such term is the electric-type quadrupole coupling,

$$S_Q \equiv -\frac{1}{2}\int \mathrm{d}\tau\, Q^{ij}(\tau)E_{ij}(\tau)\,, \tag{C.1}$$

where E_{ij} is the electric component of the Weyl tensor projected onto the spatial hypersurface of a free-falling basis,[23] and Q^{ij} is the mass quadrupole moment of the object. A similar coupling appears for the magnetic component. Higher-order multipole moments can also be easily incorporated.

The quadrupole moment can be further split into two parts: *i*) a background term, which is independent of any external perturbations, and *ii*) the response induced by an external field, for instance the gravitational field induced by a companion in a binary system. The effects of a permanent quadrupole moment depend on the scaling of Q^{ij} with the size and spin of the body. For example, the symmetric and trace-free spin-induced quadrupole moment of a rotating body can be parameterized as

$$\left(Q^{ij}\right)_S = -\frac{C_{ES^2}}{M}\left(S^iS^j - \frac{\delta^{ij}}{3}S^kS^k\right), \tag{C.2}$$

where S^i is the spin vector and C_{ES^2} is a dimensionless Wilson coefficient that incorporates the intrinsic properties of the object. The factor of $1/M$ is chosen for convenience, so that $C_{ES^2} = 1$ for Kerr BHs. This parameter is equivalent to κ, introduced in §4.2, and measures the spin-induced quadrupolar deformability of the object, relative to the value for a rotating BH with the same mass and spin. At leading order, the quadrupole term leads to the following additional term in the worldline effective action [12, 28, 33, 34]

$$S_{ES^2} = \frac{C_{ES^2}}{2M}\int \mathrm{d}\tau\, S^{ik}S^{jk}\,E_{ij}\,, \tag{C.3}$$

where S^{ij} is the spin tensor, so that $S^i = \frac{1}{2}\epsilon^{ijk}S^{jk}$. Using the power counting rules of the EFT, it is straightforward to show that this term contributes at 2PN order for binary systems with a rapidly spinning compact object (see [22] for more details).

In the presence of an external perturbation, the object's multipole moments also receive induced corrections proportional to the external field. For example, in the static limit, the response part of the quadrupole moment is[24]

$$\left(Q_{ij}\right)_R = -C_E\,E_{ij}\,, \tag{C.4}$$

[23] The electric part of the Weyl tensor W_{acbd} is defined as $E_{ab} = W_{acbd}u^cu^d$, with u^a being the four-velocity. The tetrad is chosen such that $e^a_0 = u^a$. Since $E_{ab}u^b = 0$, only the spatial indices matter in the projection to the free-falling frame $E_{ij} = e^a_i e^b_j E_{ab}$.

[24] In general, the response function depends on the frequency of the external field, with C_E being the real part in the low-frequency limit. The imaginary part of the response is responsible for the absorptive properties of the body. See [13, 14] for more details.

where we have introduced the Wilson coefficient C_E, often called the 'Love number'. In the worldline theory, this leads to the following higher-dimension term in the effective action,

$$S_{E^2} = \frac{C_E}{2} \int \mathrm{d}\tau \, E_{ij} E^{ij} \,, \tag{C.5}$$

which is quadratic in the external field. Notice that the parameter C_E scales as [mass] $\times$ [size]^4 for general bodies, and hence as [mass]^5 for compact objects. It is thus conventional to introduce the dimensionless Love number, or 'deformability parameter', as (see e.g. [5])

$$\Lambda \equiv \frac{C_E}{M^5} \,. \tag{C.6}$$

Because of the many derivatives involved, this term enters at 5PN order for compact objects in a binary system, e.g. [11]. Perhaps somewhat surprisingly, the Love numbers vanish for BHs in four-dimensional General Relativity. This unexpected 'fine tuning' offers a unique opportunity to probe the nature of spacetime, and the existence of exotic objects, through precision GW data [7].

References

[1] B. Abbott *et al.* (LIGO/Virgo Collaboration), "Observation of Gravitational Waves from a Binary Black Hole Merger," *Phys. Rev. Lett.* **116** (2016) 061102, arXiv:1602.03837 [gr-qc].

[2] B. Abbott *et al.* (LIGO/Virgo Collaboration), "GW151226: Observation of Gravitational Waves from a 22-Solar-Mass Binary Black Hole Coalescence," *Phys. Rev. Lett.* **116** (2016) 241103, arXiv:1606.04855 [gr-qc].

[3] B. Abbott *et al.* (LIGO/Virgo Collaboration), "GW170104: Observation of a 50-Solar-Mass Binary Black Hole Coalescence at Redshift 0.2," *Phys. Rev. Lett.* **118** (2017) 221101, arXiv:1706.01812 [gr-qc].

[4] B. Abbott *et al.* (LIGO/Virgo Collaboration), "GW170814: A Three-Detector Observation of Gravitational Waves from a Binary Black Hole Coalescence," *Phys. Rev. Lett.* **119** (2017) 141101, arXiv:1709.09660 [gr-qc].

[5] B. Abbott *et al.* (LIGO/Virgo Collaboration), "GW170817: Observation of Gravitational Waves from a Binary Neutron Star Inspiral," *Phys. Rev. Lett.* **119** (2017) 161101, arXiv:1710.05832 [gr-qc].

[6] B. Abbott *et al.*, "Multi-Messenger Observations of a Binary Neutron Star Merger," *Astrophys. J.* **848** (2017) L12, arXiv:1710.05833 [astro-ph.HE].

[7] R. A. Porto, "The Tune of Love and the Nature(ness) of Spacetime," *Fortsch. Phys.* **64** (2016) 723, arXiv:1606.08895 [gr-qc].

[8] R. A. Porto, "The Music of the Spheres: The Dawn of Gravitational Wave Science," arXiv:1703.06440 [physics.pop-ph].

[9] A. Buonanno and B. Sathyaprakash, "Sources of Gravitational Waves: Theory and Observations," arXiv:1410.7832 [gr-qc].

[10] C. Palenzuela, P. Pani, M. Bezares, V. Cardoso, L. Lehner, and S. Liebling, "Gravitational Wave Signatures of Highly Compact Boson Star Binaries," *Phys. Rev.* **D96** no. 10, (2017) 104058, arXiv:1710.09432 [gr-qc].

[11] W. Goldberger and I. Rothstein, "An Effective Field Theory of Gravity for Extended Objects," *Phys. Rev. D* **73** (2006) 104029, arXiv:hep-th/0409156 [hep-th].

[12] R. A. Porto, "Post-Newtonian Corrections to the Motion of Spinning Bodies in NRGR," *Phys. Rev. D* **73** (2006) 104031, arXiv:gr-qc/0511061 [gr-qc].

[13] W. Goldberger and I. Rothstein, "Dissipative Effects in the Worldline Approach to Black Hole Dynamics," *Phys. Rev. D* **73** (2006) 104030, arXiv:hep-th/0511133 [hep-th].

[14] R. A. Porto, "Absorption Effects due to Spin in the Worldline Approach to Black Hole Dynamics," *Phys. Rev. D* **77** (2008) 064026, arXiv:0710.5150 [hep-th].

[15] W. Goldberger, "Les Houches Lectures on Effective Field Theories and Gravitational Radiation," in *Les Houches Summer School - Session 86: Particle Physics and Cosmology.* 2007. arXiv:hep-ph/0701129 [hep-ph].

[16] R. A. Porto and R. Sturani, "Scalar Gravity: Post-Newtonian Corrections via an Effective Field Theory Approach," in *Les Houches Summer School - Session 86: Particle Physics and Cosmology.* 2007. arXiv:gr-qc/0701105 [gr-qc].

[17] W. Goldberger and A. Ross, "Gravitational Radiative Corrections from Effective Field Theory,"

Phys. Rev. D **81** (2010) 124015, arXiv:0912.4254 [gr-qc].

[18] A. Ross, "Multipole Expansion at the Level of the Action," *Phys. Rev. D* **85** (2012) 125033, arXiv:1202.4750 [gr-qc].

[19] S. Foffa and R. Sturani, "Effective Field Theory Methods to Model Compact Binaries," *Class. Quant. Grav.* **31** (2014) 043001, arXiv:1309.3474 [gr-qc].

[20] V. Cardoso and R. A. Porto, "Analytic Approximations, Perturbation Theory, Effective Field Theory Methods and their Applications," *Gen. Rel. Grav.* **46** (2014) 1682, arXiv:1401.2193 [gr-qc].

[21] I. Rothstein, "Progress in Effective Field Theory Approach to the Binary Inspiral Problem," *Gen. Rel. Grav.* **46** (2014) 1726.

[22] R. A. Porto, "The Effective Field Theorist's Approach to Gravitational Dynamics," *Phys. Rept.* **633** (2016) 1, arXiv:1601.04914 [hep-th].

[23] T. Binnington and E. Poisson, "Relativistic Theory of Tidal Love Numbers," *Phys. Rev. D* **80** (2009) 084018, arXiv:0906.1366 [gr-qc].

[24] T. Damour and A. Nagar, "Relativistic Tidal Properties of Neutron Stars," *Phys. Rev. D* **80** (2009) 084035, arXiv:0906.0096 [gr-qc].

[25] E. Flanagan and T. Hinderer, "Constraining Neutron Star Tidal Love Numbers with Gravitational Wave Detectors," *Phys. Rev. D* **77** (2008) 021502, arXiv:0709.1915 [astro-ph].

[26] T. Hinderer, "Tidal Love Numbers of Neutron Stars," *Astrophys. J.* **677** (2008) 1216, arXiv:0711.2420 [astro-ph].

[27] E. Poisson, "Gravitational Waves from Inspiraling Compact Binaries: The Quadrupole Moment Term," *Phys. Rev. D* **57** (1998) 5287, arXiv:gr-qc/9709032 [gr-qc].

[28] R. A. Porto and I. Rothstein, "Next-to-Leading Order Spin(1)Spin(1) Effects in the Motion of Inspiralling Compact Binaries," *Phys. Rev. D* **78** (2008) 044013, arXiv:0804.0260 [gr-qc]. [Erratum: Phys. Rev. D **81** (2010) 029905].

[29] N. Krishnendu, K. Arun, and C. Mishra, "Testing the Binary Black Hole Nature of a Compact Binary Coalescence," *Phys. Rev. Lett.* **119** (2017) 091101, arXiv:1701.06318 [gr-qc].

[30] V. Cardoso, E. Franzin, A. Maselli, P. Pani, and G. Raposo, "Testing Strong-Field Gravity with Tidal Love Numbers," *Phys. Rev. D* **95** (2017) 084014, arXiv:1701.01116 [gr-qc]. [Addendum: Phys. Rev. D **95** (2017) 089901].

[31] N. Sennett, T. Hinderer, J. Steinhoff, A. Buonanno, and S. Ossokine, "Distinguishing Boson Stars from Black Holes and Neutron Stars from Tidal Interactions in Inspiraling Binary Systems," *Phys. Rev. D* **96** (2017) 024002, arXiv:1704.08651 [gr-qc].

[32] L. Blanchet, "Gravitational Radiation from Post-Newtonian Sources and Inspiralling Compact Binaries," *Living Rev. Rel.* **17** (2014) 2, arXiv:1310.1528 [gr-qc].

[33] R. A. Porto and I. Rothstein, "The Hyperfine Einstein-Infeld-Hoffmann Potential," *Phys. Rev. Lett.* **97** (2006) 021101, arXiv:gr-qc/0604099 [gr-qc].

[34] R. A. Porto and I. Rothstein, "Spin(1)Spin(2) Effects in the Motion of Inspiralling Compact Binaries at Third Order in the Post-Newtonian Expansion," *Phys. Rev. D* **78** (2008) 044012, arXiv:0802.0720 [gr-qc]. [Erratum: Phys. Rev. D **81** (2010) 029904].

[35] R. A. Porto, "Next-to-Leading Order Spin-Orbit Effects in the Motion of Inspiralling Compact

Binaries," *Class. Quant. Grav.* **27** (2010) 205001, arXiv:1005.5730 [gr-qc].

[36] R. A. Porto, A. Ross, and I. Rothstein, "Spin-Induced Multipole Moments for the Gravitational Wave Flux from Binary Inspirals to Third Post-Newtonian Order," *JCAP* **1103** (2011) 009, arXiv:1007.1312 [gr-qc].

[37] R. A. Porto, A. Ross, and I. Rothstein, "Spin-Induced Multipole Moments for the Gravitational Wave Amplitude from Binary Inspirals to 2.5 Post-Newtonian Order," *JCAP* **1209** (2012) 028, arXiv:1203.2962 [gr-qc].

[38] M. Levi and J. Steinhoff, "Complete Conservative Dynamics for Inspiralling Compact Binaries with Spins at Fourth Post-Newtonian Order," arXiv:1607.04252 [gr-qc].

[39] S. Foffa and R. Sturani, "Dynamics of the Gravitational Two-Body Problem at Fourth Post-Newtonian Order and at Quadratic Order in the Newton Constant," *Phys. Rev. D* **87** (2013) 064011, arXiv:1206.7087 [gr-qc].

[40] T. Damour, P. Jaranowski, and G. Schäfer, "Nonlocal-In-Time Action for the Fourth Post-Newtonian Conservative Dynamics of Two-Body Systems," *Phys. Rev. D* **89** (2014) 064058, arXiv:1401.4548 [gr-qc].

[41] C. Galley, A. Leibovich, R. A. Porto, and A. Ross, "Tail Effect in Gravitational Radiation Reaction: Time Nonlocality and Renormalization Group Evolution," *Phys. Rev. D* **93** (2016) 124010, arXiv:1511.07379 [gr-qc].

[42] L. Bernard, L. Blanchet, A. Bohé, G. Faye, and S. Marsat, "Fokker Action of Nonspinning Compact Binaries at the Fourth Post-Newtonian Approximation," *Phys. Rev. D* **93** (2016) 084037, arXiv:1512.02876 [gr-qc].

[43] T. Damour, P. Jaranowski, and G. Schäfer, "Conservative Dynamics of Two-Body Systems at the Fourth Post-Newtonian Approximation of General Relativity," *Phys. Rev. D* **93** (2016) 084014, arXiv:1601.01283 [gr-qc].

[44] S. Foffa, P. Mastrolia, R. Sturani, and C. Sturm, "Effective Field Theory Approach to the Gravitational Two-Body Dynamics, at Fourth Post-Newtonian Order and Quintic in the Newton Constant," *Phys. Rev. D* **95** (2017) 104009, arXiv:1612.00482 [gr-qc].

[45] T. Damour and P. Jaranowski, "Four-Loop Static Contribution to the Gravitational Interaction Potential of Two Point Masses," *Phys. Rev. D* **95** (2017) 084005, arXiv:1701.02645 [gr-qc].

[46] R. A. Porto and I. Rothstein, "Apparent Ambiguities in the Post-Newtonian Expansion for Binary Systems," *Phys. Rev. D* **96** (2017) 024062, arXiv:1703.06433 [gr-qc].

[47] R. A. Porto, "Lamb Shift and the Gravitational Binding Energy for Binary Black Holes," *Phys. Rev. D* **96** (2017) 024063, arXiv:1703.06434 [gr-qc].

[48] T. Marchand, L. Bernard, L. Blanchet, and G. Faye, "Ambiguity-Free Completion of the Equations of Motion of Compact Binary Systems at the Fourth Post-Newtonian Order," *Phys. Rev. D* **97** (2018) 044023, arXiv:1707.09289 [gr-qc].

[49] B. Kol and M. Smolkin, "Black Hole Stereotyping: Induced Gravito-Static Polarization," *JHEP* **02** (2012) 010, arXiv:1110.3764 [hep-th].

[50] N. Gurlebeck, "No-Hair Theorem for Black Holes in Astrophysical Environments," *Phys. Rev. Lett.* **114** (2015) 151102, arXiv:1503.03240 [gr-qc].

[51] S. Endlich, V. Gorbenko, J. Huang, and L. Senatore, "An Effective Formalism for Testing Extensions to General Relativity with Gravitational Waves," *JHEP* **09** (2017) 122,

arXiv:1704.01590 [gr-qc].

[52] R. Essig *et al.*, "Working Group Report: New Light Weakly Coupled Particles," in *Community Summer Study 2013: Snowmass on the Mississippi (CSS2013) Minneapolis, MN, USA, July 29-August 6, 2013*. 2013. arXiv:1311.0029 [hep-ph].

[53] Y. Zel'Dovich, "Generation of Waves by a Rotating Body," *JETP Letters* **14** (1971) 180.

[54] Y. Zel'Dovich, "Amplification of Cylindrical Electromagnetic Waves Reflected from a Rotating Body," *Sov. Phys. JETP* **35** (1972) 1085.

[55] C. Misner, "Stability of Kerr Black Holes Against Scalar Perturbations," *Bulletin of the American Physical Society* **17** (1972) 472.

[56] A. Starobinsky, "Amplification of Waves Reflected from a Rotating "Black Hole"," *Sov. Phys. JETP* **37** (1973) 28. [Zh. Eksp. Teor. Fiz. **64** (1973) 48].

[57] A. Starobinsky and S. Churilov, "Amplification of Electromagnetic and Gravitational Waves Scattered by a Rotating "Black Hole"," *Sov. Phys. JETP* **38** (1974) 1.

[58] W. East and F. Pretorius, "Superradiant Instability and Backreaction of Massive Vector Fields around Kerr Black Holes," *Phys. Rev. Lett.* **119** (2017) 041101, arXiv:1704.04791 [gr-qc].

[59] W. East, "Superradiant Instability of Massive Vector Fields around Spinning Black Holes in the Relativistic Regime," *Phys. Rev. D* **96** (2017) 024004, arXiv:1705.01544 [gr-qc].

[60] R. Brito, V. Cardoso, and P. Pani, "Superradiance," *Lect. Notes Phys.* **906** (2015) 1, arXiv:1501.06570 [gr-qc].

[61] R. Peccei and H. Quinn, "CP Conservation in the Presence of Pseudoparticles," *Phys. Rev. Lett.* **38** (1977) 1440.

[62] S. Weinberg, "A New Light Boson?," *Phys. Rev. Lett.* **40** (1978) 223.

[63] F. Wilczek, "Problem of Strong P and T Invariance in the Presence of Instantons," *Phys. Rev. Lett.* **40** (1978) 279.

[64] L. Hui, J. Ostriker, S. Tremaine, and E. Witten, "Ultralight Scalars as Cosmological Dark Matter," *Phys. Rev. D* **95** (2017) 043541, arXiv:1610.08297 [astro-ph.CO].

[65] B. Li, T. Rindler-Daller, and P. Shapiro, "Cosmological Constraints on Bose-Einstein-Condensed Scalar Field Dark Matter," *Phys. Rev. D* **89** (2014) 083536, arXiv:1310.6061 [astro-ph.CO].

[66] P. Svrcek and E. Witten, "Axions In String Theory," *JHEP* **06** (2006) 051, arXiv:hep-th/0605206 [hep-th].

[67] D. Baumann and L. McAllister, *Inflation and String Theory*. Cambridge University Press, 2015. arXiv:1404.2601 [hep-th].

[68] A. Arvanitaki, S. Dimopoulos, S. Dubovsky, N. Kaloper, and J. March-Russell, "String Axiverse," *Phys. Rev. D* **81** (2010) 123530, arXiv:0905.4720 [hep-th].

[69] A. Arvanitaki and S. Dubovsky, "Exploring the String Axiverse with Precision Black Hole Physics," *Phys. Rev. D* **83** (2011) 044026, arXiv:1004.3558 [hep-th].

[70] W. Skiba, "Effective Field Theory and Precision Electroweak Measurements," in *Physics of the Large and the Small, Proceedings of TASI 09, Boulder, Colorado, USA, 1-26 June 2009*. 2011. arXiv:1006.2142 [hep-ph].

[71] N. Arkani-Hamed and J. Maldacena, "Cosmological Collider Physics," arXiv:1503.08043 [hep-th].

[72] X. Chen and Y. Wang, "Quasi-Single-Field Inflation and Non-Gaussianities," *JCAP* **1004** (2010) 027, arXiv:0911.3380 [hep-th].

[73] D. Baumann and D. Green, "Signatures of Supersymmetry from the Early Universe," *Phys. Rev.* **D85** (2012) 103520, arXiv:1109.0292 [hep-th].

[74] V. Assassi, D. Baumann, and D. Green, "On Soft Limits of Inflationary Correlation Functions," *JCAP* **1211** (2012) 047, arXiv:1204.4207 [hep-th].

[75] X. Chen and Y. Wang, "Quasi-Single-Field Inflation with Large Mass," *JCAP* **1209** (2012) 021, arXiv:1205.0160 [hep-th].

[76] T. Noumi, M. Yamaguchi, and D. Yokoyama, "Effective Field Theory Approach to Quasi-Single-Field Inflation and Effects of Heavy Fields," *JHEP* **06** (2013) 051, arXiv:1211.1624 [hep-th].

[77] V. Assassi, D. Baumann, D. Green, and L. McAllister, "Planck-Suppressed Operators," *JCAP* **1401** (2014) 033, arXiv:1304.5226 [hep-th].

[78] R. Flauger, D. Green, and R. A. Porto, "On Squeezed Limits in Single-Field Inflation. Part I," *JCAP* **1308** (2013) 032, arXiv:1303.1430 [hep-th].

[79] H. Lee, D. Baumann, and G. Pimentel, "Non-Gaussianity as a Particle Detector," *JHEP* **12** (2016) 040, arXiv:1607.03735 [hep-th].

[80] D. Baumann, G. Goon, H. Lee, and G. L. Pimentel, "Partially Massless Fields During Inflation," arXiv:1712.06624 [hep-th].

[81] S. Kumar and R. Sundrum, "Heavy-Lifting of Gauge Theories By Cosmic Inflation," arXiv:1711.03988 [hep-ph].

[82] H. An, M. McAneny, A. Ridgway, and M. Wise, "Quasi-Single-Field Inflation in the Nonperturbative Regime," arXiv:1706.09971 [hep-ph].

[83] G. Raffelt, *Stars as Laboratories for Fundamental Physics*. University of Chicago Press, Chicago, IL, 1996.

[84] K. Abazajian (CMB-S4 Collaboration), "CMB-S4 Science Book, First Edition," arXiv:1610.02743 [astro-ph.CO].

[85] D. Baumann, D. Green, and B. Wallisch, "New Target for Cosmic Axion Searches," *Phys. Rev. Lett.* **117** (2016) 171301, arXiv:1604.08614 [astro-ph.CO].

[86] C. Brust, D. Kaplan, and M. Walters, "New Light Species and the CMB," *JHEP* **12** (2013) 058, arXiv:1303.5379 [hep-ph].

[87] J. Bekenstein and M. Schiffer, "The Many Faces of Superradiance," *Phys. Rev. D* **58** (1998) 064014, arXiv:gr-qc/9803033 [gr-qc].

[88] W. Press and S. Teukolsky, "Floating Orbits, Superradiant Scattering and the Black Hole Bomb," *Nature* **238** (1972) 211.

[89] W. Unruh, "Separability of the Neutrino Equations in a Kerr Background," *Phys. Rev. Lett.* **31** (1973) 1265.

[90] B. Carter, "Hamilton-Jacobi and Schrödinger Separable Solutions of Einstein's Equations," *Commun. Math. Phys.* **10** (1968) 280.

[91] D. Brill *et al.*, "Solution of the Scalar Wave Equation in a Kerr Background by Separation of Variables," *Phys. Rev. D* **5** (1972) 1913.

[92] S. Dolan, "Instability of the Massive Klein-Gordon Field on the Kerr Spacetime," *Phys. Rev. D* **76** (2007) 084001, arXiv:0705.2880 [gr-qc].

[93] S. Detweiler, "Klein-Gordon Equation and Rotating Black Holes," *Phys. Rev. D* **22** (1980) 2323.

[94] P. Pani, V. Cardoso, L. Gualtieri, E. Berti, and A. Ishibashi, "Perturbations of Slowly Rotating Black Holes: Massive Vector Fields in the Kerr Metric," *Phys. Rev. D* **86** (2012) 104017, arXiv:1209.0773 [gr-qc].

[95] H. Yoshino and H. Kodama, "Gravitational Radiation from an Axion Cloud around a Black Hole: Superradiant Phase," *PTEP* **2014** (2014) 043E02, arXiv:1312.2326 [gr-qc].

[96] R. Brito *et al.*, "Gravitational Wave Searches for Ultralight Bosons with LIGO and LISA," *Phys. Rev. D* **96** (2017) 064050, arXiv:1706.06311 [gr-qc].

[97] D. Christodoulou, "Reversible and Irreversible Transformations in Black-Hole Physics," *Phys. Rev. Lett.* **25** (1970) 1596.

[98] B. Abbott *et al.* (LIGO/Virgo Collaboration), "Astrophysical Implications of the Binary Black-Hole Merger GW150914," *Astrophys. J.* **818** (2016) L22, arXiv:1602.03846 [astro-ph.HE].

[99] R. Brito, V. Cardoso, and P. Pani, "Black Holes as Particle Detectors: Evolution of Superradiant Instabilities," *Class. Quant. Grav.* **32** (2015) 134001, arXiv:1411.0686 [gr-qc].

[100] P. Landry and E. Poisson, "Tidal Deformation of a Slowly Rotating Material Body. External Metric," *Phys. Rev. D* **91** (2015) 104018, arXiv:1503.07366 [gr-qc].

[101] X.-H. Zhang, "Multipole Expansions of the General-Relativistic Gravitational Field of the External Universe," *Phys. Rev. D* **34** (1986) 991.

[102] S. Taylor and E. Poisson, "Nonrotating Black Hole in a Post-Newtonian Tidal Environment," *Phys. Rev. D* **78** (2008) 084016, arXiv:0806.3052 [gr-qc].

[103] P. Eggleton, "Approximations to the Radii of Roche Lobes," *Astrophys. J.* **268** (1983) 368.

[104] P. Peters, "Gravitational Radiation and the Motion of Two Point Masses," *Phys. Rev.* **136** (1964) B1224.

[105] A. Arvanitaki, M. Baryakhtar, and X. Huang, "Discovering the QCD Axion with Black Holes and Gravitational Waves," *Phys. Rev. D* **91** (2015) 084011, arXiv:1411.2263 [hep-ph].

[106] A. Arvanitaki, M. Baryakhtar, S. Dimopoulos, S. Dubovsky, and R. Lasenby, "Black Hole Mergers and the QCD Axion at Advanced LIGO," *Phys. Rev. D* **95** (2017) 043001, arXiv:1604.03958 [hep-ph].

[107] K. Riles, "Recent Searches for Continuous Gravitational Waves," *Mod. Phys. Lett. A* **32** (2017) 1730035, arXiv:1712.05897 [gr-qc].

[108] R. Hulse and J. Taylor, "Discovery of a Pulsar in a Binary System," *Astrophys. J.* **195** (1975) L51.

[109] J. Aasi *et al.* (LIGO Scientific Collaboration), "First All-Sky Search for Continuous Gravitational Waves from Unknown Sources in Binary Systems," *Phys. Rev. D* **90** (2014) 062010, arXiv:1405.7904 [gr-qc].

[110] R. Geroch, "Multipole Moments. II. Curved Space," *J. Math. Phys.* **11** (1970) 2580.

[111] R. Hansen, "Multipole Moments of Stationary Spacetimes," *J. Math. Phys.* **15** (1974) 46.

[112] B. Carter, "Axisymmetric Black Hole Has Only Two Degrees of Freedom," *Phys. Rev. Lett.* **26** (1971) 331.

[113] D. Robinson, "Uniqueness of the Kerr Black Hole," *Phys. Rev. Lett.* **34** (1975) 905.

[114] W. Laarakkers and E. Poisson, "Quadrupole Moments of Rotating Neutron Stars," *Astrophys. J.* **512** (1999) 282, arXiv:gr-qc/9709033 [gr-qc].

[115] G. Pappas and T. Apostolatos, "Revising the Multipole Moments of Numerical Spacetimes, and its Consequences," *Phys. Rev. Lett.* **108** (2012) 231104, arXiv:1201.6067 [gr-qc].

[116] F. Ryan, "Spinning Boson Stars with Large Self-Interaction," *Phys. Rev. D* **55** (1997) 6081.

[117] V. Kalogera and G. Baym, "The Maximum Mass of a Neutron Star," *Astrophys. J.* **470** (1996) L61, arXiv:astro-ph/9608059 [astro-ph].

[118] C. Herdeiro and E. Radu, "Kerr Black Holes with Scalar Hair," *Phys. Rev. Lett.* **112** (2014) 221101, arXiv:1403.2757 [gr-qc].

[119] R. Penrose, "Gravitational Collapse: the Role of General Relativity," *Riv. Nuovo Cim.* **1** (1969) 252. [Gen. Rel. Grav. 34 (2002) 1141].

[120] P. Pani, L. Gualtieri, A. Maselli, and V. Ferrari, "Recent Progress on the Tidal Deformability of Spinning Compact Objects," *Proceedings of the 14th Marcel Grossmann Meeting* (2017) 1587.

[121] R. Mendes and H. Yang, "Tidal Deformability of Boson Stars and Dark Matter Clumps," *Class. Quant. Grav.* **34** (2017) 185001, arXiv:1606.03035 [astro-ph.CO].

[122] T. Damour, "The Problem of Motion in Newtonian and Einsteinian Gravity," in *300 Years of Gravitation, S. Hawking and W. Israel, eds., pp. 128-198. Cambridge University Press.* 1987.

[123] J. Aasi *et al.* (LIGO Scientific Collaboration), "Advanced LIGO," *Class. Quant. Grav.* **32** (2015) 074001, arXiv:1411.4547 [gr-qc].

[124] F. Acernese *et al.* (VIRGO Collaboration), "Advanced Virgo: a Second-Generation Interferometric Gravitational Wave Detector," *Class. Quant. Grav.* **32** (2015) 024001, arXiv:1408.3978 [gr-qc].

[125] K. Somiya *et al.* (KAGRA Collaboration), "Detector Configuration of KAGRA: The Japanese Cryogenic Gravitational-Wave Detector," *Class. Quant. Grav.* **29** (2012) 124007, arXiv:1111.7185 [gr-qc].

[126] B. Sathyaprakash *et al.*, "Scientific Objectives of Einstein Telescope," *Class. Quant. Grav.* **29** (2012) 124013, arXiv:1206.0331 [gr-qc]. [Erratum: Class. Quant. Grav. **30** (2013) 079501].

[127] B. Abbott *et al.* (LIGO Scientific Collaboration), "Exploring the Sensitivity of Next Generation Gravitational Wave Detectors," *Class. Quant. Grav.* **34** (2017) 044001, arXiv:1607.08697 [astro-ph.IM].

[128] P. Amaro-Seoane *et al.*, "eLISA/NGO: Astrophysics and Cosmology in the Gravitational-Wave Millihertz Regime," *GW Notes* **6** (2013) 4, arXiv:1201.3621 [astro-ph.CO].

[129] S. Kawamura *et al.*, "The Japanese Space Gravitational Wave Antenna: DECIGO," *Class. Quant. Grav.* **28** (2011) 094011.

[130] P. Graham *et al.* (MAGIS Collaboration), "Mid-Band Gravitational Wave Detection with Precision Atomic Sensors," arXiv:1711.02225 [astro-ph.IM].

[131] G. Hobbs, "The Parkes Pulsar Timing Array," *Class. Quant. Grav.* **30** (2013) 224007, arXiv:1307.2629 [astro-ph.IM].

[132] M. Kramer and D. Champion, "The European Pulsar Timing Array and the Large European Array for Pulsars," *Class. Quant. Grav.* **30** (2013) 224009.

[133] M. McLaughlin, "The North American Nanohertz Observatory for Gravitational Waves," *Class.*

Quant. Grav. **30** (2013) 224008, arXiv:1310.0758 [astro-ph.IM].

[134] R. Manchester, "The International Pulsar Timing Array," *Class. Quant. Grav.* **30** (2013) 224010, arXiv:1309.7392 [astro-ph.IM].

[135] R. Smits, M. Kramer, B. Stappers, D. Lorimer, J. Cordes, and A. Faulkner, "Pulsar Searches and Timing with the Square Kilometre Array," *Astron. Astrophys.* **493** (2009) 1161, arXiv:0811.0211 [astro-ph].

[136] G. Hobbs, S. Dai, R. Manchester, R. Shannon, M. Kerr, K. Lee, and R. Xu, "The Role of FAST in Pulsar Timing Arrays," arXiv:1407.0435 [astro-ph.IM].

[137] B. Abbott *et al.* (LIGO/Virgo Collaboration), "The Rate of Binary Black Hole Mergers Inferred from Advanced LIGO Observations Surrounding GW150914," *Astrophys. J.* **833** (2016) L1, arXiv:1602.03842 [astro-ph.HE].

[138] G. Nelemans, S. Portegies Zwart, F. Verbunt, and L. Yungelson, "Population Synthesis for Double White Dwarfs. 2. Semi-Detached Systems: AM CVN Stars," *Astron. Astrophys.* **368** (2001) 939, arXiv:astro-ph/0101123 [astro-ph].

[139] K. Belczynski, M. Benacquista, and T. Bulik, "Double Compact Objects as Low-Frequency Gravitational Wave Sources," *Astrophys. J.* **725** (2010) 816, arXiv:0811.1602 [astro-ph].

[140] A. Lamberts *et al.*, "Predicting the Binary Black Hole Population of the Milky Way with Cosmological Simulation," arXiv:1801.03099 [astro-ph.GA].

[141] J. Gair, L. Barack, T. Creighton, C. Cutler, S. Larson, S. Phinney, and M. Vallisneri, "Event Rate Estimates for LISA Extreme Mass Ratio Capture Sources," *Class. Quant. Grav.* **21** (2004) S1595, arXiv:gr-qc/0405137 [gr-qc].

[142] A. Sesana, "Prospects for Multiband Gravitational-Wave Astronomy after GW150914," *Phys. Rev. Lett.* **116** (2016) 231102, arXiv:1602.06951 [gr-qc].

[143] L. Barack, "Gravitational Self Force in Extreme Mass-Ratio Inspirals," *Class. Quant. Grav.* **26** (2009) 213001, arXiv:0908.1664 [gr-qc].

[144] C. Galley and R. A. Porto, "Gravitational Self-Force in the Ultra-Relativistic Limit: the "Large-N" Expansion," *JHEP* **11** (2013) 096, arXiv:1302.4486 [gr-qc].

[145] L. Barack and C. Cutler, "Using LISA EMRI Sources to Test Off-Kerr Deviations in the Geometry of Massive Black Holes," *Phys. Rev. D* **75** (2007) 042003, arXiv:gr-qc/0612029 [gr-qc].

[146] D. Baumann *et al.*, *work in progress*.